

## Invariant-mass spectroscopy of $^{18}\text{Ne}$ , $^{16}\text{O}$ , and $^{10}\text{C}$ excited states formed in neutron-transfer reactions

R. J. Charity, K. W. Brown, J. Elson, W. Reviol, and L. G. Sobotka

*Departments of Chemistry and Physics, Washington University, St. Louis, Missouri 63130, USA*

W. W. Buhro, Z. Chajecski,\* W. G. Lynch, J. Manfredi, R. Shane, R. H. Showalter, M. B. Tsang,  
D. Weisshaar, and J. Winkelbauer

*National Superconducting Cyclotron Laboratory and Department of Physics and Astronomy,  
Michigan State University, East Lansing, Michigan 48824, USA*

S. Bedoor

*Department of Physics, Western Michigan University, Kalamazoo, Michigan 49008, USA*

D. G. McNeel and A. H. Wuosmaa

*Department of Physics, Western Michigan University, Kalamazoo, Michigan 49008, USA  
and Department of Physics, University of Connecticut, Storrs, Connecticut 06269, USA*



(Received 2 October 2018; published 9 April 2019)

Neutron-transfer reactions with fast secondary beams of  $^{17}\text{Ne}$ ,  $^{15}\text{O}$ , and  $^9\text{C}$  have been studied with the HiRA and CAESAR arrays. Excited states of  $^{18}\text{Ne}$ ,  $^{16}\text{O}$ , and  $^{10}\text{C}$  in the continuum have been identified using invariant-mass spectroscopy. The best experimental resolution of these states is achieved by selecting events where the decay fragments are emitted transverse to the beam direction. We have confirmed a number of spin assignments made in previous works for the negative-parity states of  $^{18}\text{Ne}$ . In addition we have found new higher-lying excited states in  $^{16}\text{O}$  and  $^{18}\text{Ne}$ , some of which fission into two ground-state  $^8\text{Be}$  fragments. Finally for  $^{10}\text{C}$ , a new excited state was observed. These transfer reactions were found to leave the remnant of the  $^9\text{Be}$  target nuclei at very high excitation energies and may be associated with the pickup of a deeply bound  $^9\text{Be}$  neutron.

DOI: [10.1103/PhysRevC.99.044304](https://doi.org/10.1103/PhysRevC.99.044304)

### I. INTRODUCTION

Invariant-mass spectroscopy with fast radioactive beams has proven a valuable tool for studying the structure of light exotic isotopes near the drip lines. With the High Resolution Array (HiRA) [1], we have focused our studies on states produced in nucleon knockout reactions for isotopes near and beyond the proton drip line [2–6]. However in the same experiments, we also obtained data for a number of other reactions types [3,7]. In this work we will report on levels obtained from neutron-transfer reactions with fast  $^{17}\text{Ne}$ ,  $^{15}\text{O}$ , and  $^9\text{C}$  secondary beams using experimental data sets for which knockout results have already been published. One advantage of the invariant-mass technique is its selectivity to the decay channel. This allows one to isolate small cross sections associated with exotic exit channels and determine branching ratios in decays.

The experimental technique will be validated by studying the well-known spectroscopy of  $^{16}\text{O}$  states which can be produced with the  $^{15}\text{O}$  beam. In particular we will look at

the  $\alpha$ -particle branching ratio for the  $J^\pi = 2_3^-$  level which is important to determine its isospin mixing with the neighboring  $J^\pi = 2_2^-$  level [8]. With the  $^{17}\text{Ne}$  beam, we will look at the low-lying levels of  $^{18}\text{Ne}$ . The structure of  $^{18}\text{Ne}$  has attracted considerable interest due to its importance for the resonant component of the  $^{14}\text{O}(\alpha, p)^{17}\text{F}$  and  $^{17}\text{F}(p, \gamma)^{18}\text{Ne}$  reactions in astrophysics [9–11]. In the course of such studies, Hahn *et al.* [9] produced an evaluated level scheme for this isotope and made spin assignments based on the level widths, cross sections, and angular distributions in various reactions, and Thomas-Ehrman shifts relative to the mirror  $^{18}\text{O}$  system. Due to the selectivity of transfer reactions, only levels of certain spins and parity will be strongly populated with a  $^{17}\text{Ne}$  beam and this can be used to check the spin assignments of Hahn *et al.* In addition, for all three projectiles, we will look for previously unobserved higher-lying excited states. Here the power of the invariant-mass technique will allow us to observe highly fragmented decay channels with interesting decay modes.

Our main interest is the low-lying particle-unstable states formed by neutron capture to the  $p$  and  $sd$  shells. However, from semiclassical models of this process [12], transfer of a nucleon to such orbitals with fast beams ( $E/A = 60\text{--}70$  MeV) is poorly matched in terms of linear and angular-momentum

\*Present address: Department of Physics, Western Michigan University, Kalamazoo, Michigan 49008, USA.

transfer leading to small cross sections. Moreover, transfer reactions also have selectivity to structures with single-particle-like configurations and can be used to probe such structures and constrain models. Indeed at lower energies where linear and angular momentum are better matched, transfer reactions such as  $(d, p)$  have contributed significantly to this area using the missing-mass technique. Such cases are amenable to simple reaction theory (distorted wave Born approximation for instance) and spectroscopic strengths and spin assignments can be inferred from the detected cross sections and angular distributions. However with fast secondary beams, the missing-mass technique requires thinner targets than those typically used with the invariant-mass technique. In addition, because of the large phase space of these secondary beams, beam tracking is required for the determination of absolute angles. On the other hand, only relative angles are important in the invariant-mass technique making it insensitive to the beam quality.

In this work we will explore the role that the invariant-mass technique can play in these transfer reactions and present its advantages and disadvantages. Finally this work is complementary to recent studies using  $\gamma$ -ray spectroscopy following transfer reactions with fast secondary beams where the final projectilelike fragment is detected in a spectrometer [13–15].

## II. EXPERIMENTAL METHOD

The data presented in this work were obtained from experiments performed at the Coupled Cyclotron Facility at the National Superconducting Cyclotron Laboratory at Michigan State University. Details of these experiments have been described in Refs. [4–6] and only a brief description will be given here. A secondary beam of intensity  $1.5 \times 10^5$  pps was obtained from the fragmentation of an  $E/A = 170$ -MeV  $^{20}\text{Ne}$  primary beam (80 pA). This beam contained  $^{17}\text{Ne}$  (11%) and  $^{15}\text{O}$  (80%) with energies in the center of a 1-mm-thick Be target of  $E/A = 58.2$  and  $48.1$  MeV, respectively. In a separate experiment, a secondary beam of intensity  $9 \times 10^4$  pps was obtained from an  $E/A = 150$ -MeV  $^{16}\text{O}$  primary beam (175 pA). This beam contained  $^9\text{C}$  at the 52% level with an energy in the center of the same target of  $E/A = 64.6$  MeV. The other main component of this beam was  $^6\text{Li}$ .

Charged particles produced from reactions with the target were detected in the High Resolution Array (HiRA) [1] consisting of 14  $\Delta E - E$  telescopes arranged around the beam to cover zenith angles from  $2^\circ$  to  $13.9^\circ$ . The double-sided Si strip  $\Delta E$  detectors permitted accurate determination of the scattering angles of the detected fragments. The heavier fragments ( $A > 10$ ) were only identified in the central two telescopes where the  $\Delta E$  strips were set up with dual gains. Energy calibrations of the CsI(Tl)  $E$  detectors were achieved using a series of cocktail beams including  $E/A = 55$ - and  $75$ -MeV protons and  $N = Z$  fragments, and  $E/A = 73.4$ - and  $95.2$ -MeV  $^7\text{Be}$  fragments. Other fragments such as  $^{15}\text{N}$  and  $^{17}\text{F}$  have only a single calibration point each at  $E/A = 40.1$  and  $51.3$  MeV, respectively. In these cases, we use this calibration point to define effective thicknesses of the Si  $\Delta E$  detectors and then use energy-loss tables [16] to determine  $E$  from the  $\Delta E$  measurement. The relative locations of each

HiRA telescope and the target were determined very accurately using a coordinate measurement machine arm.

The CAESAR (CAESium iodide ARray) detector [17] was positioned to surround the target in order to detect  $\gamma$  rays emitted in coincidence with charged particles. For this experiment, the array consisted of 158 CsI(Na) crystals covering polar angles between  $57.5^\circ$  and  $122.4^\circ$  in the laboratory frame with complete azimuthal coverage. The first and last rings of the full CAESAR array were removed due to space constraints.

For the normalization of cross sections, the number of beam particles was determined by counting using a thin plastic-scintillator foil placed in the focal point of the A1900 fragment separator. For the  $^{17}\text{Ne}$ - $^{15}\text{O}$  beam, the loss in the beam flux due to its transport to the target and the relative contribution from each beam species was determined by temporarily placing a CsI(Tl) detector just after the target position. These fluxes were also corrected for the detector dead time measured with a random pulse generator. No similar calibrations were performed for the  $^9\text{C}$  beam. Here we rely on a previous experiment with the same beam energy, target, and detector setup where a similar calibration was performed [3]. Normalization of cross sections in the present case was determined by reproducing the value for  $^8\text{C}_{g.s.}$  from the previous experiment. The uncertainties quoted for the cross sections in the remainder of this work are statistical only. In addition, systematic uncertainties of  $\pm 15\%$  for the  $^{18}\text{Ne}$  and  $^{16}\text{O}$  states and  $\pm 20\%$  for the  $^{10}\text{C}$  states have been assigned.

## III. INVARIANT-MASS METHOD

For a group of detected fragments believed to be the decay products of a nuclear level, we can calculate its excitation energy as

$$E_{n\gamma}^* = E_{\text{inv}} - E_{g.s.} \quad (1)$$

where  $E_{\text{inv}}$  is the invariant mass of the fragments and  $E_{g.s.}$  is the ground-state mass of the decaying nucleus. However, the quantity  $E_{n\gamma}^*$  is only the true excitation energy if no  $\gamma$  rays were emitted in the decay. For example, the particle decay of a state may leave one or both of the decay fragments in particle-bound excited states which subsequently  $\gamma$  decay. In such cases, the true excitation energy is obtained by adding the  $\gamma$ -ray energies, i.e.,

$$E^* = E_{n\gamma}^* + \sum_i E_i^\gamma \quad (2)$$

The use of the CAESAR  $\gamma$ -ray array allows us to identify such cases and apply this correction.

The experimental apparatus is only sensitive to particle decays of projectilelike states which are produced at laboratory angles close to the beam axis ( $\theta_{\text{lab}} < 10^\circ$ ). For two-body decays where the invariant mass can be determined solely from the relative velocity between the two fragments, the experimental resolution depends very strongly on the decay direction. For example, Fig. 1 shows the simulated resolution (see the Appendix) expressed as a full width at half maximum (FWHM) of the invariant-mass peak for the decay  $^{18}\text{Ne} \rightarrow p + ^{17}\text{F}$  with an excitation energy of 5.135 MeV and zero intrinsic width. The angle  $\theta$  is the emission angle of

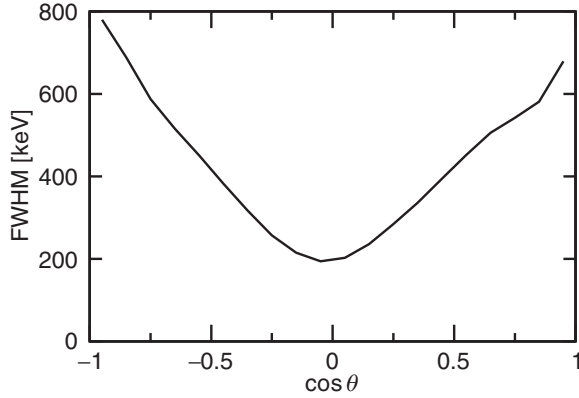


FIG. 1. Simulated  $^{18}\text{Ne} \rightarrow p + ^{17}\text{F}$  resolution expressed as the FWHM of the invariant-mass distribution for a level with zero intrinsic width and  $E^* = 5.135$  MeV. Results are shown as a function of the  $\theta$ , the emission angle of the proton in the  $^{18}\text{Ne}^*$  frame where  $\theta = 0^\circ$  corresponds to emission along the beam axis.

the proton in the  $^{18}\text{Ne}^*$  center-of-mass frame with  $\theta = 0^\circ$  corresponding to emission along the beam axis. This strong angular dependence reflects the fact that we have excellent relative-angle resolution, but poorer energy resolution, and the relative contribution of these to the total resolution is strongly  $\theta$  dependent. In both cases, these resolutions are dominated by the effect of the thick target. For the relative-angular resolution, it is the small-angle scattering of the decay products in the target material which is important, while for the energy resolution, the uncertainty in the interaction depth in the target leads to an uncertainty in the energy loss of the decay fragments as they leave the target.

For transverse decays ( $\cos\theta \sim 0$ ), uncertainties in the energies of the detected fragments act perpendicular to the decay axis and thus only contribute to the invariant-mass uncertainty in second order. In this case, the experimental resolution is dominated by the angular resolution. On the other hand for longitudinal decays ( $|\cos\theta| \sim 1$ ), the angular uncertainty contributes in second order and the experimental resolution is now dominated by the contribution from the energy. If there are enough statistics, it is clearly advantageous to restrict the analysis to events which decay transversely. For example, Fig. 2 shows the inclusive (data points) and transverse-gated ( $|\cos\theta| < 0.2$ , histograms) invariant-mass spectra for detected  $p + ^{15}\text{N}$  and  $p + ^{17}\text{F}$  events. Both spectra show a number of peaks associated with  $^{16}\text{O}$  and  $^{18}\text{Ne}$  levels and our ability to resolve and identify these is clearly superior with the transverse gate. The transverse gate  $|\cos\theta| < 0.2$  will be used in the following work unless otherwise specified.

For similar reasons, the transverse-gated spectra also have reduced sensitivity to errors in the CsI(Tl) energy calibrations, thus reducing the systematic uncertainty in the fitted peak energies. To estimate the magnitude of this uncertainty we have fitted nine invariant-mass peaks associated with proton decay of  $^{12,13,14,15}\text{N}$  and  $^{14,15}\text{O}$  levels which have small intrinsic widths and their decay energies are well known. The weighted mean deviation from the ENSDF [18] decay

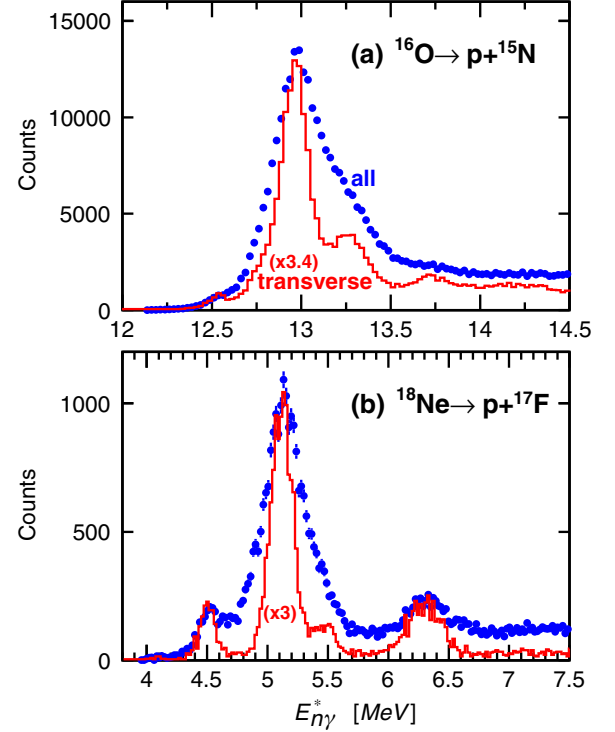


FIG. 2. Experimental excitation-energy spectra obtained with the invariant-mass method from detected (a)  $p + ^{15}\text{N}$  and (b)  $p + ^{17}\text{F}$  events. The data points were obtained from all detected events, while the histograms are for transverse decays only ( $|\cos\theta| < 0.2$ ).

energies is  $-1.5(33)$  keV. Thus we chose a  $2\sigma$  deviation of 6.6 keV as a reasonable choice for this systematic uncertainty.

#### IV. REACTION MECHANISM

To better understand the possible states which may be present in the invariant-mass spectra, one should consider the reaction mechanism. In this work we analyze multiparticle coincidences where the sum of the  $Z$  and  $N$  of the fragments are consistent with the breakup of a parent nucleus with one more neutron than a beam particle. For example the circular data points in Fig. 3 show the center-of-mass velocity distribution of  $p + ^{17}\text{F}$  pairs obtained with the  $^{17}\text{Ne}$  beam. This velocity spectrum, typical of other cases we observe, has a prominent peak at  $\sim 90\%$  of the beam velocity with a low-velocity tail. These pairs can come from the decay  $^{18}\text{Ne}$  parents produced from single neutron-transfer reactions or from the sequential decay of heavy systems in multinuclear exchange reactions. If the latter is true, then other sequential decay fragments should also be present and, apart from neutrons, will be detected. The square and triangular data points in Fig. 3 are from detected  $2p + ^{17}\text{F}$  and  $p + \alpha + ^{17}\text{F}$  events. The center-of-mass velocity of the  $p + ^{17}\text{F}$  pairs in these triple-coincident events are plotted. If the extra particles in these two channels were not detected then such events can contribute to the detected  $p + ^{17}\text{F}$  events. Based on our Monte Carlo simulations of detection efficiencies, the yield in these two channels has been scaled so as to represent the contamination in the  $p + ^{17}\text{F}$  spectrum from these higher-multiplicity channels. Integrating

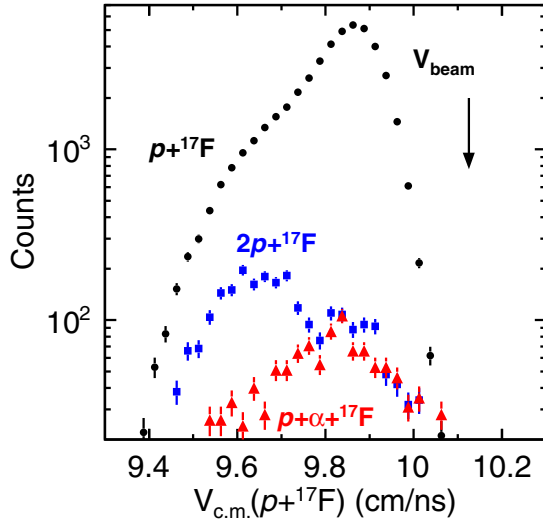


FIG. 3. Center-of-mass velocity distributions of  $p + {}^{17}\text{F}$  pairs obtained with the  ${}^{17}\text{Ne}$  beam. The circular data points are for detected pairs, while the square and triangular points are estimations of the contribution from  $2p + {}^{17}\text{F}$  and  $p + \alpha + {}^{17}\text{F}$  events where only a  $p + {}^{17}\text{F}$  is detected. The beam velocity is indicated by the arrow.

the spectra, the contamination from the  $2p + {}^{17}\text{F}$  ( $p + \alpha + {}^{17}\text{F}$ ) channel is  $\sim 5\%$  ( $\sim 2\%$ ) and the contribution from other higher-multiplicity channels is considerably smaller. Thus the production of  $p + {}^{17}\text{F}$  resonances by sequential charged-particle emission from a heavier system is insignificant.

The spectral shape of these two contaminants' distribution is different from the  $p + {}^{17}\text{F}$  events with broader distributions lacking the prominent peak at  $\sim 9.85$  cm/ns. In fact, the  $2p + {}^{17}\text{F}$  events contribute more to the low-velocity tail. The spectral shape of the contamination from  $p + n + {}^{17}\text{F}$  events will probably be similar and thus will not be able to explain the yield in the prominent peak. Therefore we believe that these events are predominately produced by a single neutron transfer to the projectile, with the low-velocity tail possibly having more significant contributions from multinucleons transfers.

Similar center-of-mass velocity distributions are shown in Fig. 4 for the parent nuclei obtained with each beam species with the addition of a neutron. We have also included in Fig. 4(d) the  $\alpha + \alpha$  channel obtained with a  ${}^7\text{Be}$  beam with the same experimental setup and target [2]. These spectra are all gated on a prominent peak in the associated invariant-mass spectra (see caption for details). This gating reduces the relative magnitude of the low-velocity tail, possibly diminishing the relative importance of a nonresonant background in the invariant-mass spectra. The widths of the experimental peaks have large contributions from the experimental resolution associated with the range of interaction depths in the target material. This is especially true for the heavier beams. It is therefore best to focus our attention on the centroid of the peaks. The expected velocity of the parent systems based on two-body kinematics for a one-neutron-transfer reaction is shown by the solid vertical lines when the  ${}^8\text{Be}$  target remnant is left in its ground state. All the experimental distributions peak at a velocity slightly below this value suggesting the

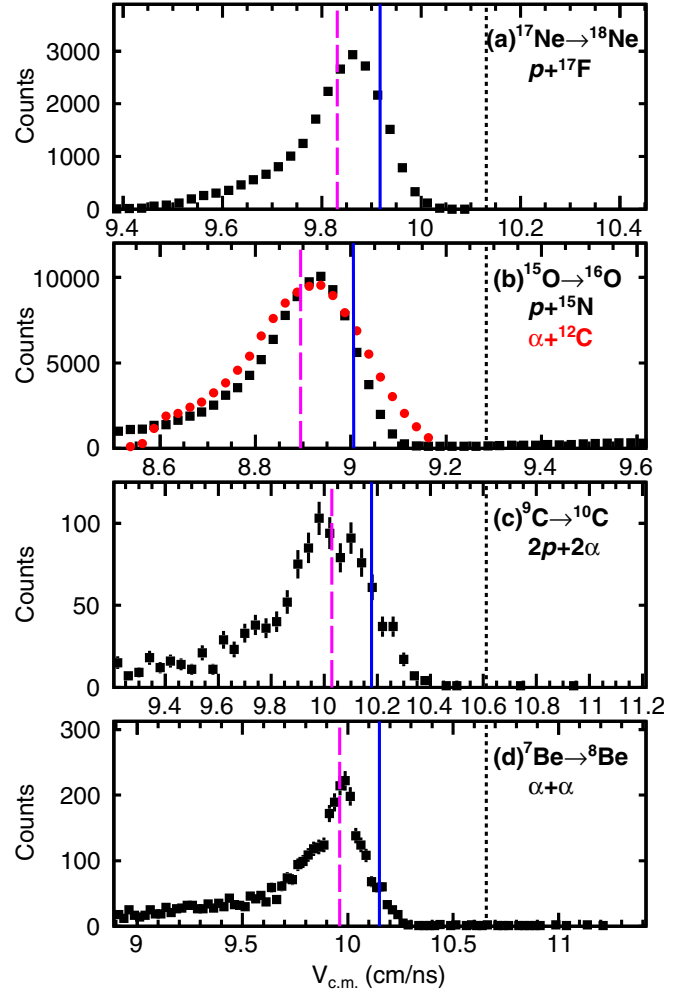


FIG. 4. Center-of-mass velocity distributions for the indicated exit channels associated with the transfer of a neutron to (a)  ${}^{17}\text{Ne}$ , (b)  ${}^{15}\text{O}$ , (c)  ${}^9\text{C}$ , and (d)  ${}^7\text{Be}$  beam particles. Each distribution is gated on a prominent peak in the associated invariant-mass spectrum. These are (a) the 5.135-MeV state in  ${}^{18}\text{Ne}$  (Sec. VI), (b) the 12.969-plus 13.250-MeV doublet in  ${}^{16}\text{O}$  for both  $p_0$  and  $\alpha_1$  decay channels (Sec. V), (c) the 9.69-MeV state in  ${}^{10}\text{C}$  (Sec. VII), and (d) the ground and  $2^+$  excited state in  ${}^8\text{Be}$ . For comparison, the beam velocities are indicated by the dotted lines. The velocities expected from two-body kinematics if the  ${}^8\text{Be}$  target remnant is left in its ground state or with 20 MeV of excitation are shown by the solid and dashed lines, respectively.

remnant is left excited. The long-dashed vertical lines for instance show the predicted locations if the remnant has an excitation energy of 20 MeV. If the  ${}^9\text{Be}$  target nucleus is considered as a valence neutron with a deformed  ${}^8\text{Be}$  core, then it appears that a neutron from the core is preferentially transferred, rather than the valence neutron.

In the study of neutron-transfer reactions with a  ${}^{22}\text{Mg}$  fragmentation beam using  $\gamma$ -ray spectroscopy, Gade *et al.* concluded that the yields obtained with a  ${}^9\text{Be}$  target were too large to be explained by the pickup of the weakly bound  ${}^9\text{Be}$  valence neutron [14]. From the measured longitudinal momentum distribution of the final projectile fragments, they

conclude that these transfer reactions were not two body in nature, i.e., the projectile and target after the transfer were not both left in well-defined excited states. In addition they inferred that the reactions with the  $^9\text{Be}$  target were dominated by the pickup of one of the deeply bound neutrons which would lead to  $E_{\text{target}}^* \sim 20$  MeV. This is qualitatively consistent with our observations. Gade *et al.* also studied transfer reactions with a  $^{12}\text{C}$  target and found a very different result. Here the yields were found to be consistent with a two-body reaction mechanism and a coupled-channel-Born-approximation calculation was able to reproduce the measured cross sections.

### V. $^{16}\text{O}$ EXCITED STATES

Neutron pickup by the  $^{15}\text{O}$  beam provides an excellent test of our understanding of transfer reactions at these higher energies as the  $^{16}\text{O}$  states of interest are well characterized and one can compare to lower-energy data from the mirror reaction, proton transfer to  $^{15}\text{N}$  [19,20]. The ground-state configuration of  $^{16}\text{O}$  consists predominantly of a neutron hole in the  $p$  shell. In neutron-transfer reactions, the lower-energy states are produced by either filling this hole and making a  $J^\pi = 0^+$  state, or, by capturing the neutron into the  $sd$  shell. Of these possibilities, neutron capture to either the  $d_{5/2}$  or  $d_{3/2}$  level forming  $J^\pi = 1^-, 2^-$ , or  $3^-$  states will have the smaller momentum mismatch and thus are expected to produce the largest cross sections at these energies. Capture to the  $pf$  shell will generally produce states of larger excitation energy where the level density increases and our experimental resolution is poorer making it generally more difficult to isolate and identify them.

Invariant-mass spectra for the  $p + ^{15}\text{N}$  and  $\alpha + ^{12}\text{C}$  transverse decay channels of  $^{16}\text{O}$  formed with the  $^{15}\text{O}$  beam are plotted in Figs. 5(a) and 5(b). The observed peaks for  $p + ^{15}\text{N}$  are all associated with decay to the ground state of  $^{15}\text{N}$  apart from the highest-energy one ( $E_{n\gamma}^* \sim 13.7$  MeV) which will be discussed later (Sec. V B). The  $\gamma$ -ray spectrum in coincidence with the detected  $\alpha + ^{12}\text{C}$  pairs is shown in the inset in Fig. 5(c) where a peak associated with the  $E_\gamma = 4.438$ -MeV  $\gamma$  ray from the decay of the first excited state of  $^{12}\text{C}$  is visible. Below this, the first escape peak is also clearly evident. Using the  $\gamma$ -ray gate indicated in the inset of Fig. 5(c), which encompasses both peaks, the resulting  $^{16}\text{O}$  excitation-energy spectrum is shown Fig. 5(c). Comparing this  $\gamma$ -gated and the inclusive spectra of Fig. 5(b), one finds both are almost identical in shape below  $E^* = 10$  MeV but not above and thus the lower-energy peak structures must be associated with decays to the first excited state of  $^{12}\text{C}$ , while the higher-energy structures observed in Fig. 5(b) are associated with decays to the ground state.

Both the  $p + ^{15}\text{N}$  and  $\alpha + ^{12}\text{C}$  invariant-mass spectra have been fitted with peaks from the  $^{16}\text{O}$  levels that were observed in the lower-energy proton-transfer experiments with  $^{15}\text{N}$  targets [19,20]. The peak energies and intrinsic widths were fixed to their values in [18], while their intensities and a smooth background are varied to reproduce the data. Detector resolution is included via the Monte Carlo simulations (see the Appendix). The results are shown by the solid-red curves with

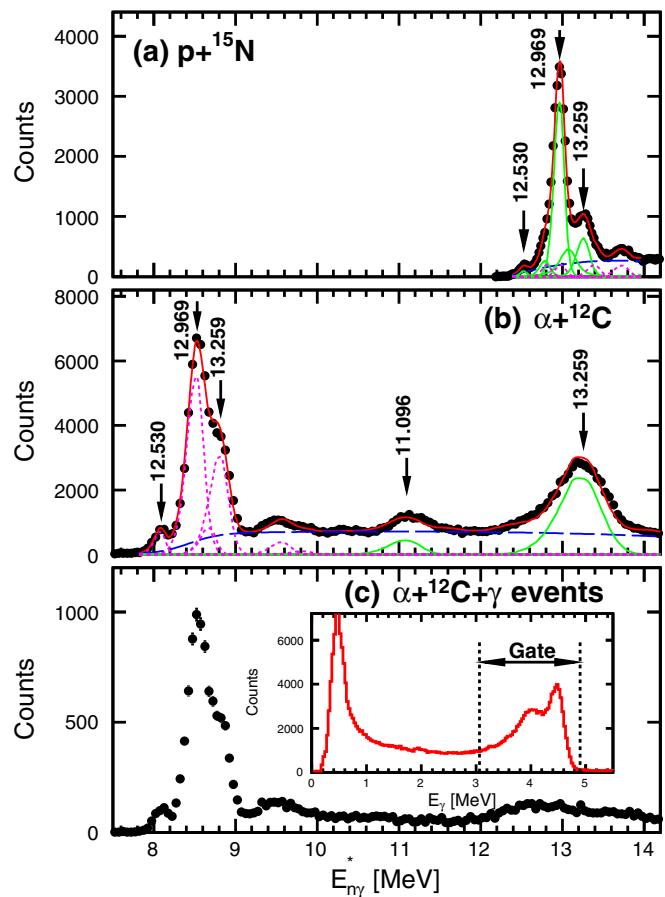


FIG. 5. Distribution of  $^{16}\text{O}$  excitation energy reduced by the total energies of emitted  $\gamma$  rays for events detected with the  $^{15}\text{O}$  beam. (a),(b) Data points show the experimental distribution for all detected  $p + ^{15}\text{N}$  and  $\alpha + ^{12}\text{C}$  pairs, respectively. The solid-red curves show fits to these distributions using known  $^{16}\text{O}$  levels. The individual contributions from these levels are shown as the solid curves for decays to the respective ground states. In (b), decays to the first excited state of  $^{12}\text{C}$  are indicated by the dotted curves. Background contributions (dash-blue curve) were also included in the fit. (c) Excitation-energy spectrum gated on  $\gamma$  rays from the decay of the first excited state of  $^{12}\text{C}$ . The inset shows the Doppler-corrected  $\gamma$  spectrum measured in coincidence with  $\alpha + ^{12}\text{C}$  pairs and the gate used to select  $\gamma$  rays from the decay of this excited state.

individual components indicated by the solid (green) curves for decay to the ground state or dashed (magenta) curves for decay to the excited state. Note that for the  $\alpha + ^{12}\text{C}_{\text{g.s.}}$  decay channel, no  $J^\pi = 0^-, 2^-$  levels are considered as such decays would violate parity conservation. These fits show that both spectra are dominated by the decay of two  $T = 1$  states: the  $J^\pi = 3_3^-$  state at  $E^* = 13.259$  MeV observed in the  $p_0$ ,  $\alpha_0$ , and  $\alpha_1$  channels and a  $J^\pi = 2_3^-$  state ( $E^* = 12.969$  MeV) observed in the  $p_0$  and  $\alpha_1$  channels. In addition the  $T = 0$ ,  $J^\pi = 2_2^-$  state at  $E^* = 12.530$  MeV is observed at lower intensity in the  $p + ^{15}\text{N}$  and  $\alpha + ^{12}\text{C}_{4.438 \text{ MeV}}$  channels. Finally there is evidence for a peak at  $E^* = 11.096$  MeV in the  $\alpha + ^{12}\text{C}_{\text{g.s.}}$  channel at low yield which corresponds to a  $J^\pi = 3^+$  state, involving the capture of a  $f$ -shell neutron. The fits confirm

our expectation that states formed by neutron capture to the  $d$  orbitals dominate. Also, the experimental spectra were fit without any significant contribution from the  $E^* = 10.957$ - and  $12.796$ -MeV  $J^\pi = 0^-$  states and the  $E^* = 12.440$ - and  $13.090$ -MeV  $J^\pi = 1^-$  states which all involve capture to the second  $s_{1/2}$  level even though their spectroscopic factors are significant [20]. This suppression of  $s_{1/2}$  capture is consistent with a larger momentum mismatch at these higher bombarding energies.

### A. Branching ratio of $J^\pi = 2_3^-$ level

The  $J^\pi = 2^-$  states at  $E^* = 12.530$  MeV ( $T = 0$ ) and  $12.969$  MeV ( $T = 1$ ) are close enough in energy that there is some isospin mixing. The magnitude of this mixing can be determined from their  $\alpha$ -particle reduced widths [8]. However there is a disagreement in the value of the partial widths or branching ratios for the ( $T = 1$ )  $12.969$ -MeV state. Historically, the first information on this branching ratio is from the compilation of Ajzenberg-Selove [21] giving  $\Gamma_{\alpha 1}/\Gamma = 0.36(5)$ . This value was referenced to a paper of Rolf and Rodney [22] where the branching ratio is not given or discussed, so details of the derivation of this value are unknown. Later Leavitt *et al.* measured a similar value of  $0.37(6)$  from which they extracted a mixing parameter and the charge-dependent matrix element [8]. Subsequently Zijderhand and Van der Leun [23] measured a smaller value of  $0.22(4)$  which is in disagreement with the two previous measurements. It is this final value that is listed in the current Evaluated Nuclear Structure Data File (ENSDF) evaluation [18].

The  $12.969$ -MeV  $J = 2_2^-$  and  $13.259$ -MeV  $J = 3_3^-$  states form a doublet in both the  $p_0$  and  $\alpha_1$  channels in Figs. 5(a) and 5(b). Although their yields can be separated for transverse decay, this is not the case for longitudinal decay where the experimental resolution is much poorer. To obtain the branching ratios for these two states we have fit the combined  $d\sigma/d\cos\theta$  angular distributions associated with this doublet for all three observed channels ( $p_0$ ,  $\alpha_0$ , and  $\alpha_1$ ), but at the same time enforcing our experimental decomposition obtained for transverse decay. Figures 6(a)–6(c) show these combined angular distributions and their transverse decompositions are indicated by the data points with larger horizontal error bars. The shapes of the individual angular distributions for each component are defined by the  $m$ -state or magnetic-substate probability distributions  $P_m^{J^\pi}$  of the  $2_2^-$  and  $3_3^-$  states. As we have taken the beam axis as our quantization axis, then  $P_m^{J^\pi} = P_{-m}^{J^\pi}$  leaving only five free parameters if these distribution are each normalized to unity.

Following the  $R$ -matrix analysis of many data for these two levels, the decay orbital angular momentum for all the exit channels is taken to be the lowest value possible from parity and angular-momentum conservation [24–26]. For instance, both  $\alpha_1$  branches are  $\ell = 1$  and their angular distributions can be described by a constant plus a  $\cos^2\theta$  term. This criterion does not completely constrain the  $p_0$  branch of the  $2^-$  level which can be either  $d_{3/2}$  or  $d_{5/2}$ . We have allowed for an admixture of these two components plus an interference term in the fit. The total number of free parameters in the fit including the phase of the interference term is 11. With such

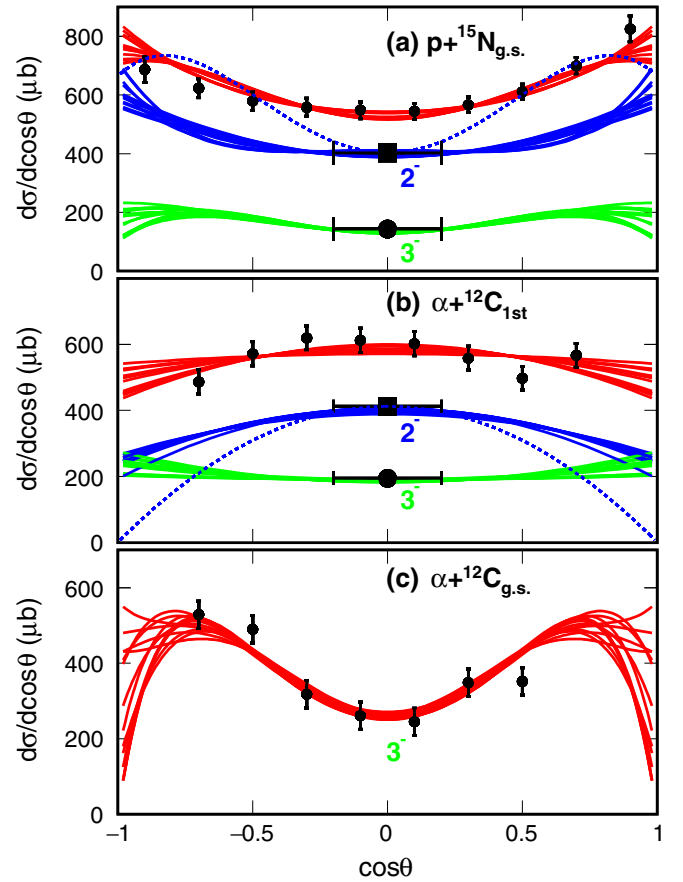


FIG. 6. Efficiency-corrected angular distribution of the decay particle in the parent  $^{16}\text{O}$  fragment center-of-mass frame for the (a)  $p_0$ , (b)  $\alpha_1$ , and (c)  $\alpha_0$  decay channels for the  $12.969$ -MeV  $J = 2_2^-$  and  $13.259$ -MeV  $J = 3_3^-$  doublet. Only the  $3_3^-$  level can contribute to the  $\alpha_0$  branch. The decomposition of this yield for transverse decay is shown as the data points with the large horizontal error bars in (a) and (b). The solid curves show the sum and individual angular distribution obtained from a large number of fits to these data. The dotted curves in (a) and (b) represent angular distributions that provide maximum and minimum yields for the  $p_0$  and  $\alpha_1$  branches, respectively.

a large number of free parameters it is not surprising that there are ambiguities, with many parameter sets producing equally good fits. Indeed the  $P_m^{J^\pi}$  distribution is not well constrained and similarly for the  $d_{3/2}$ ,  $d_{5/2}$  admixture of the  $2^-$  level. However in spite of this, the angular distributions for the individual components are rather well constrained. The curves in Figs. 6(a)–6(c) show the total and individual contributions of the angular distributions from a large number of fits obtained by sampling the multidimensional space of the free parameters. We also find that the decomposition of the  $p_0$  and  $\alpha_1$  channels is insensitive to the experimental  $\alpha_0$  angular distribution.

The extracted branching ratios for the  $3^-$  level compare well to previous values inferred from  $R$ -matrix analyses in Table I. This gives us further confidence in the extracted branching ratios for the  $2^-$  state. The extracted  $\alpha_1$  branching ratio for this state is  $0.46(8)$  which is consistent with the

TABLE I. Comparison of branching ratios for the  $3_3^-$  state in  $^{16}\text{O}$  extracted in this work compared to values obtained by  $R$ -matrix analyses of Hebbard [26] and Bray *et al.* [25].

Decay	This work	Hebbard	Bray <i>et al.</i>
$p_0$	0.22(5)	0.20	0.15
$\alpha_0$	0.47(5)	0.47	0.50
$\alpha_1$	0.30(5)	0.33	0.34

value of 0.36(6) from Leavitt *et al.*, but inconsistent with that from Zijderhand and Van der Leun which is listed in the ENSDF evaluation. Indeed it is simple to show that the value 0.22(4) obtained by Zijderhand and Van der Leun is not compatible with our data. The minimum possible total yield for the  $\alpha_1$  branch of the  $2^-$  state consistent with our extracted transverse yield can be obtained with an angular distribution

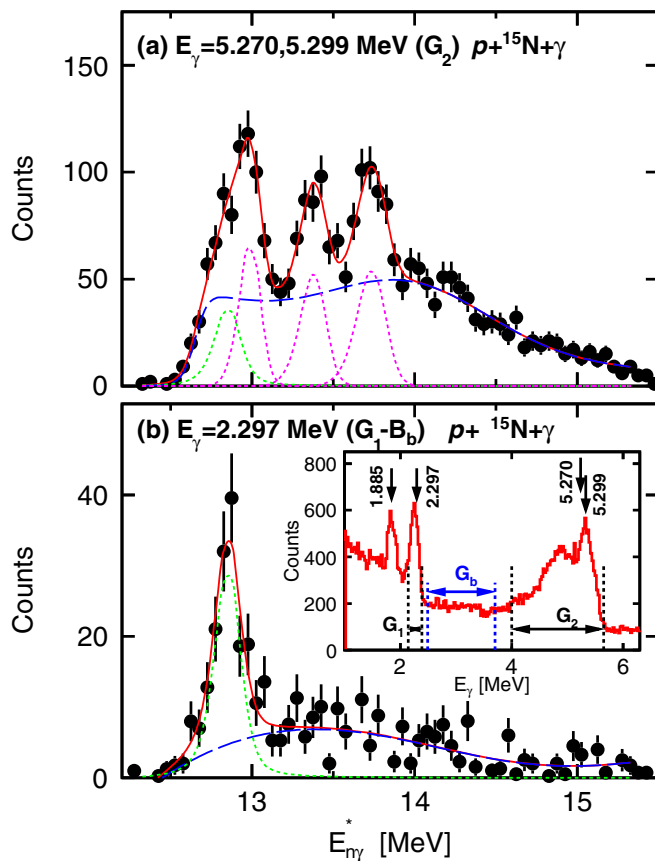


FIG. 7. Distribution of  $^{16}\text{O}$  excitation energy reduced by the total energies of  $^{15}\text{N}$   $\gamma$  rays for  $p + ^{15}\text{N}$  pairs detected with the  $^{15}\text{O}$  beam. Data points show the experimental distributions, while solid-red curves show fits to these data. The dashed-blue curves indicate the fitted background. The inset shows the Doppler-corrected  $\gamma$ -ray spectrum for all detected  $p + ^{15}\text{N}$  pairs with the energies of known  $\gamma$  rays indicated with the arrows. (a) Distribution gated on the  $G_2$  gate shown in the inset. (b) Background-subtracted distribution gated on the  $G_1$  gate in the inset. As the 2.297-MeV  $\gamma$ -ray sits on a significant background, the events in the  $G_b$  gate, suitably scaled in magnitude, were used to remove this background.

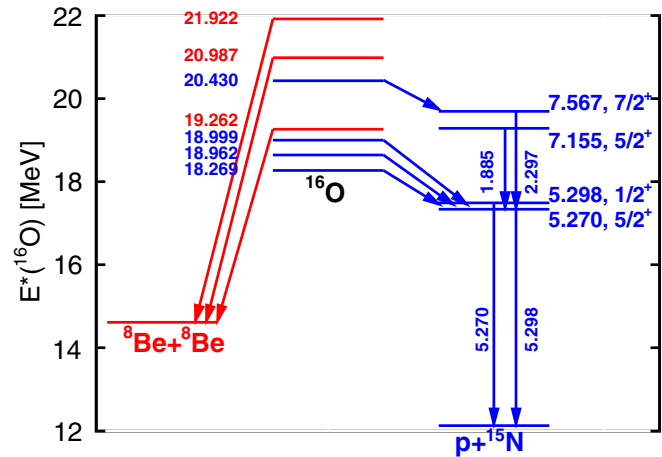


FIG. 8. Decay scheme of the newly found high-lying states in  $^{16}\text{O}$  obtained from fits to the  $p + ^{15}\text{N} + \gamma$  and  $^8\text{B}_{\text{g.s.}} + ^8\text{Be}_{\text{g.s.}}$  exit channels of  $^{16}\text{O}$ .

proportional to  $1 - \cos^2\theta$  [dotted curve in Fig. 6(b)]. For the  $p_0$  branch, as the decay is  $\ell = 2$ , the angular distribution can contain even powers of  $\cos\theta$  up to  $\cos^4\theta$ . The dotted curve in Fig. 6(b) shows the angular distribution with the largest  $p_1$  yield consistent with the extracted transverse yield, but not exceeding the total yield from the  $2_2^- - 3_3^-$  doublet. With these maximum and minimum values, we obtain a minimum branching ratio of 0.32 which exceeds the value of Zijderhand and Van der Leun.

### B. $p + ^{15}\text{N} + \gamma$ exit channels

The  $\gamma$ -ray spectrum measured in coincidence with detected  $p + ^{15}\text{N}$  pairs is displayed in the inset in Fig. 7(b). A peak at  $E_\gamma \sim 5.28$  MeV and its first escape shoulder are observed. These events can be associated with either the first ( $E^* = 5.270$  MeV,  $J^\pi = 5/2_1^+$ ) or second ( $E^* = 5.298$  MeV,  $J^\pi = 1/2_1^+$ ) excited state of  $^{15}\text{N}$ . In addition we see peaks at 1.885 and 2.297 MeV that are produced in the decay of the  $E^* = 7.155$ -MeV,  $J^\pi = 5/2_2^+$  and  $E^* = 7.567$ -MeV,  $J^\pi = 7/2_1^+$  excited states, respectively. For reference, a partial level scheme of  $^{15}\text{N}$  is shown in Fig. 8.

The excitation-energy spectrum for events in coincidence with either the 5.270- or 5.298-MeV  $\gamma$  ray (gate  $G_2$  in Fig. 7) is plotted in Fig. 7(a). Three clear peak structures are observed and the solid curve shows the results of a fit. The lower-energy peak has been fit as a doublet where the energy and width of the lower-energy member are constrained with a second  $\gamma$  gate. This second gate ( $G_1$ ) is around the 2.297-MeV  $\gamma$  ray [gate  $G_1$  in Fig. 7(b)] and we used the adjacent higher-energy  $\gamma$  rays [gate  $G_b$  in Fig. 7(b)] to estimate the background under this peak. The background-subtracted spectrum is displayed in Fig. 7(b) and only the lower-energy member of the doublet is now present as demonstrated in our fit (curve). Clearly this lower-energy member of the doublet is associated with the 7.567-MeV,  $J^\pi = 7/2_1^+$  excited state of  $^{15}\text{N}$  which decays by emitting both 2.297- and 5.270-MeV  $\gamma$  rays. The deduced

TABLE II. Parameters for the levels in  $^{16}\text{O}$  obtained from the fitting the  $\gamma$ -gated  $p + ^{15}\text{N}$  excitation-energy distributions in Fig. 7. These include the fitted centroid of each peak  $E_{n\gamma}$  and its excitation energy  $E^*$  when the  $\gamma$ -rays energies are included, and finally the fitted intrinsic width  $\Gamma$ .

$E_{n\gamma}^*$ (MeV)	$E^*$ (MeV)	$\Gamma$ (keV)
12.863(14)	20.430(14)	77(38)
12.993(11)	18.269(11)	<30 <sup>a</sup>
13.373(12)	18.643(12)	<60 <sup>a</sup>
13.729(12)	18.999(12)	<40 <sup>a</sup>

<sup>a</sup>1 $\sigma$  limit.

total excitation energies, including the  $\gamma$ -ray contributions, are listed in Table II and the decays are illustrated in Fig. 8.

### C. Four- $\alpha$ exit channels

A large number of  $4\alpha$  events were detected with the mixed  $^{15}\text{O}/^{17}\text{Ne}$  beam, but the invariant-mass spectrum for all events did not show any significant peak structures. However, such events can be obtained from a number of different decay scenarios and one interesting possibility is the fission of  $^{16}\text{O}$  into two ground-state  $^8\text{Be}$  fragments. Such events are easy to separate by looking at the momentum correlations between the  $\alpha$  particles. We have selected events where the relative energy between one pair of  $\alpha$  particles is consistent with  $^8\text{Be}$  decay and similarly for the remaining pair. The relative energy distribution is very sharply peaked for  $\alpha$  pairs from the decay of  $^8\text{Be}$  and we find there is almost no background under it. Therefore  $^8\text{Be}_{\text{g.s.}} + ^8\text{Be}_{\text{g.s.}}$  decay can be isolated cleanly. The excitation-energy spectrum for such events is displayed in Fig. 9 and shows a large peak at 19.26 MeV plus a broader structure at  $\sim 21$  MeV. The latter was fit as a doublet in Fig. 9 where the widths of two members were taken as equal. Fitted decay widths and cross sections are listed in Table III and the decay scheme is also illustrated in Fig. 8. The cross section in this and other tables were obtained by assuming isotropic

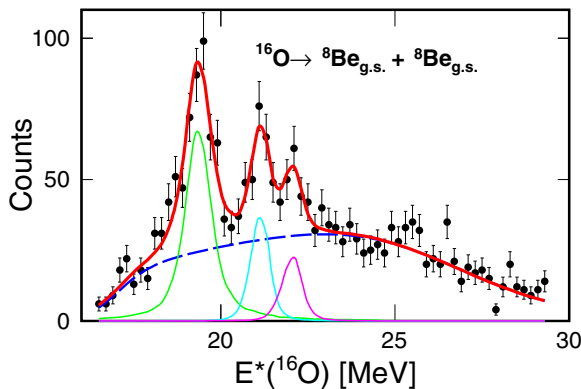


FIG. 9. Excitation-energy spectrum for the  $^8\text{Be}_{\text{g.s.}} + ^8\text{Be}_{\text{g.s.}}$  exit channel obtained from detected  $4\alpha$  events. The thick-red-solid curve shows a fit to this distribution with three levels (thin solid curves) and a smooth background (dashed-blue curve).

TABLE III. Mean excitation energies  $E^*$ , intrinsic widths  $\Gamma$ , and peak cross sections obtained for the  $^{16}\text{O}$  levels decaying to the  $^8\text{Be}_{\text{g.s.}} + ^8\text{Be}_{\text{g.s.}}$  channel observed in Fig. 9.

$E^*$ (MeV)	$\Gamma$ (keV)	$\sigma_{\text{peak}}$ ( $\mu\text{b}$ )
19.262(38)	435(151)	29(18)
20.987(52) <sup>a</sup>	57(256)	14(6)
21.922(87) <sup>a</sup>		

<sup>a</sup>Doublet.

decay in the extrapolation of the extracted transverse yields to other decay angles. As such they should be considered as rough estimates. As the decay channel consists of two identical  $J = 0$  Bosons, then these states must have positive parity and even values of  $J$ .

The reaction mechanism for the production of these states is not clear. The cross section listed in Table III assumes they were created from interactions with  $^{15}\text{O}$  beam fragments, but if they result from reactions with the less-intense  $^{17}\text{Ne}$  beam component, then the cross sections should be larger. Whichever beam component is the source of these states, at least one neutron must be transferred to the projectile to account for the total neutron number of the channel. If the  $^{17}\text{Ne}$  beam is the source, then one might suspect these  $^{16}\text{O}$  states were produced from heavier parents that sequentially proton decayed. However no significant yield of coincidence protons was obtained. In an analysis similar to that used in Fig. 3, we found that the contribution from  $p + 4\alpha$  and  $5\alpha$  events to the  $^8\text{Be}_{\text{g.s.}} + ^8\text{Be}_{\text{g.s.}}$  yield was  $\sim 1.5\%$  and  $\sim 6\%$ , respectively, and contribution from other higher-multiplicity channels to be significantly less. The  $4\alpha$  center-of-mass velocities associated with these states have a broad distribution with a peak around 8.3 cm/ns which is very low compared the distribution of the other  $^{16}\text{O}$  decay channels in Fig. 4(b). If these states are formed in simple one-neutron transfer from the target to a  $^{15}\text{O}$  beam particle, then the  $^8\text{Be}$  target remnant must be produced with an excitation energy of  $\sim 100$  MeV to achieve these low center-of-mass velocities. Possibly multineutron transfer to the  $^{15}\text{O}$  projectiles, followed by sequential neutron emission, contributes.

The  $^8\text{Be}_{\text{g.s.}} + ^8\text{Be}_{\text{g.s.}}$  exit channel of  $^{16}\text{O}$  has been investigated in a number of other studies [27–33] and a significant number of levels have been found. Our 19.26(4)-MeV peak may be associated with the 19.35-MeV peak originally identified by Chevallier *et al.* [27] in the  $^{12}\text{C}(^4\text{He}, ^8\text{Be})^8\text{Be}$  reaction where they assigned a spin of  $J^\pi = 6^+$  from the measured angular distributions. Subsequently, Freer *et al.* identified a peak in the  $^{12}\text{C}(^{16}\text{O}, ^8\text{Be} + ^8\text{Be})^{12}\text{C}$  reaction at 19.3 MeV and assigned a spin of  $J^\pi = 4^+$  [31]. Later Curtis *et al.* remeasured the  $^{12}\text{C}(^4\text{He}, ^8\text{Be})^8\text{Be}$  reaction with better resolution and the 19.3-MeV peak was found to be a doublet (19.29 and 19.36 MeV) [33]. They argued that this doublet is actually an interference effect and corresponds to a narrow resonance with either  $J^\pi = 2^+$  or  $4^+$ . The fitted intrinsic width of our peak is  $\Gamma = 435(151)$ ;  $2.9\sigma$  away from zero. In addition, according to Freer *et al.*, the 19.3-MeV

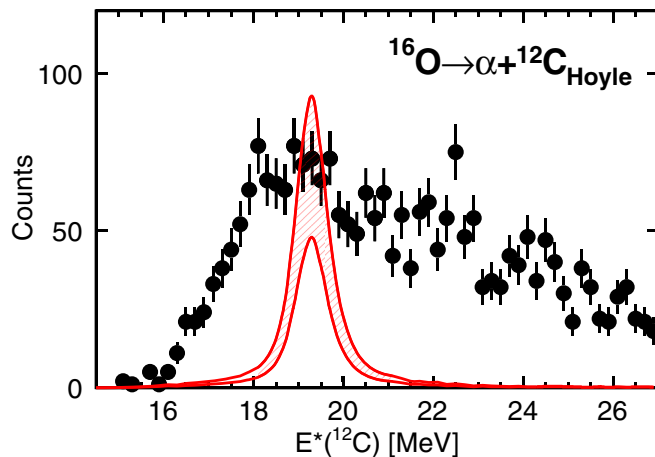


FIG. 10. Excitation-energy spectrum for the  $\alpha + {}^{12}\text{C}_{\text{Hoyle}}$  exit channel obtained from detected  $4\alpha$  events. The hatched region shows the simulated range of yields from the 19.262-MeV state assuming the branching ratio and error given in [30].

states decay more strongly to the  $\alpha + {}^{12}\text{C}(0_2^+)$  channel with  $\Gamma_{8\text{Be}}/\Gamma_{12\text{C}(0_2^+)} = 0.47(15)$ .

We can also relatively cleanly gate on such decays from our detected  $4\alpha$  events by selecting out those where three of the four  $\alpha$  particles has an invariant mass associated with the Hoyle state [ ${}^{12}\text{C}(0_2^+)$ ] state. The excitation-energy spectra are displayed as the data points in Fig. 10. For comparison, the two curves separated by the hatched region are simulated results using our best-fit intrinsic width for the 19.262-MeV state and incorporating the experimental resolution. The magnitudes of the two curves are chosen to give the experimental outer limits of the branching ratio given by Freer *et al.* Clearly the experimental spectrum does not show such a peak and the branching strength to this channel must be at least a factor of 4 smaller than that given by Freer *et al.* Probably our peak is associated with a different  ${}^{16}\text{O}$  excited state. In the work of Curtis *et al.* [33], a 21.10-MeV level was observed and assigned  $J^\pi = 4^+$  or  $6^+$  and this is consistent with our 20.987(6)-MeV peak.

## VI. $^{18}\text{Ne}$ EXCITED STATES

The  $^{18}\text{Ne}$  level scheme evaluated by Hahn *et al.* [9] is shown in Fig. 11 and compared to that for the  $^{18}\text{O}$  mirror. Some of these states can be produced by neutron capture to the  ${}^{17}\text{Ne}$  beam. The  ${}^{17}\text{Ne}$  ground-state wave function ( $J^\pi = 1/2_1^-$ ) consists predominantly of two protons in the  $sd$  shell, coupled to zero spin, and a single neutron hole in the  $p$  shell [34]. If the captured neutron fills this hole, then a  $J^\pi = 0^+$  state in  $^{18}\text{Ne}$  is formed. Otherwise neutron capture to the  $sd$  shell will produce negative-parity states. Given that the momentum mismatch will favor capture to the  $d_{3/2}$  and  $d_{5/2}$  levels, this reaction should predominantly populate  $J^\pi = 1^-, 2^-,$  and  $3^-$  states. Other positive-parity states can be populated by capture to the  $pf$  shell, but these will have larger excitation energies, where the level density is greater, making separation of the individual levels more difficult.

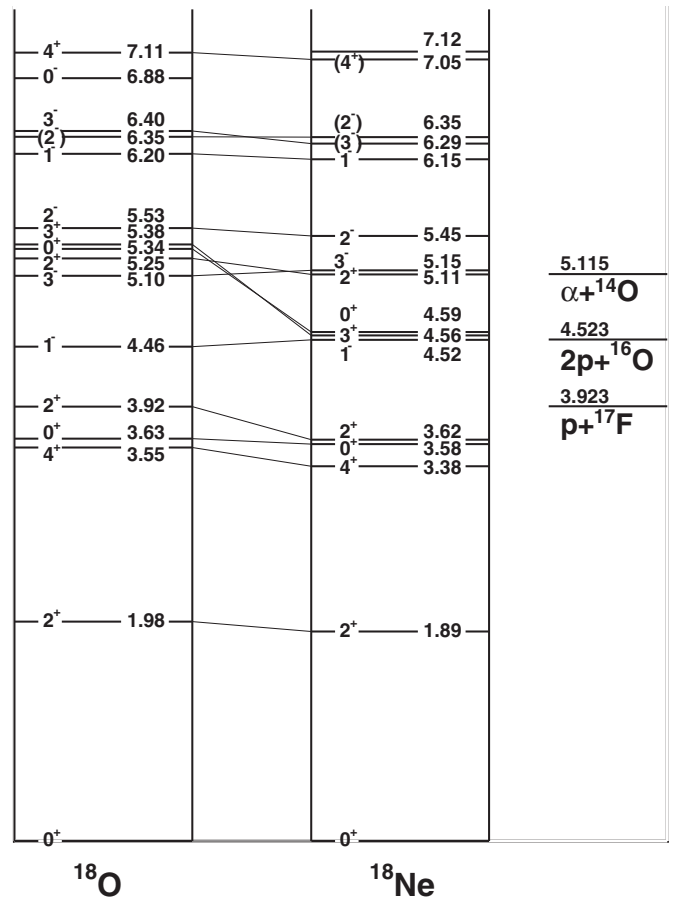


FIG. 11. Level scheme of  $^{18}\text{Ne}$  and its mirror  $^{18}\text{O}$  as given by Hahn *et al.* [9].

The  $E_{n\gamma}^*$  distribution for transverse proton decay of  $^{18}\text{Ne}$  is shown in Fig. 12. The residual  ${}^{17}\text{F}$  nucleus has one particle-bound excited state at 495 keV so attention must be given to the possibility of decay through this state. The Doppler-corrected  $\gamma$ -ray spectrum coincident with  $p + {}^{17}\text{F}$  events is shown in Fig. 13(a) as the red-solid histogram where add-back contributions from neighboring elements are included. In comparison, the green-dashed histogram represents an estimate of the background under this spectrum which was obtained from  $\gamma$  rays coincident with the prolific  $2p + {}^{15}\text{O}$  decay channel associated with the second excited state of  ${}^{17}\text{Ne}$  [7]. This  ${}^{17}\text{Ne}$  state does not produce  $\gamma$  rays so only a background contribution is present. This background spectrum was normalized to give the same yield for  $E_\gamma > 0.8$  MeV as that for the detected  $p + {}^{17}\text{F}$  pairs. It is clear that, relative to this background, the  $p + {}^{17}\text{F}$  events have an important contribution from the 495-keV  $\gamma$  ray.

The excitation-energy spectrum, shown as the data points in Fig. 13(b), is gated on the 495-keV  $\gamma$  ray using the  $E_\gamma$  limits indicated by the dashed-vertical lines in Fig. 13(a). It should be compared to the inclusive spectra (blue histogram) which is normalized to the same maximum value and both were obtained requiring  $|\cos\theta| < 0.7$  to increase statistics. Given that there is background under the 495-keV peak, then

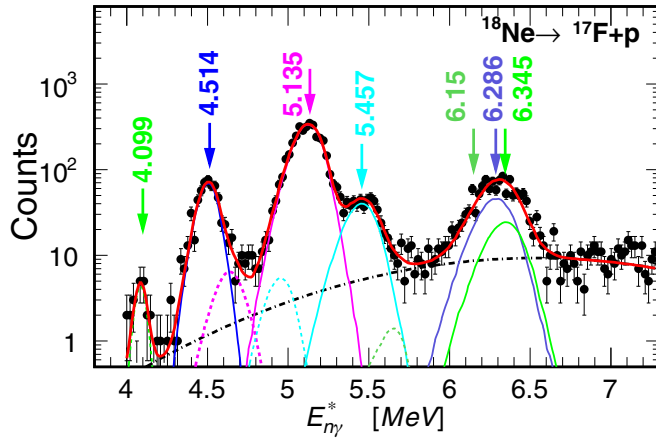


FIG. 12. Distribution of  $^{18}\text{Ne}$  excitation energy reduced by the total energies of emitted  $^{17}\text{F}$   $\gamma$  rays for  $p + ^{17}\text{F}$  pairs detected with the  $^{17}\text{Ne}$  beam. The experimental results are indicated by the data points. The thick-red curve shows a fit to this distribution, where individual contributions are also indicated. For each state in the fit, two peaks are included associated with decay to the ground (solid thin curves) and first excited state (dashed thin curves) of  $^{17}\text{F}$ . The dot-dashed curve shows a background contribution introduced to reproduce the background in the 7-MeV region. The arrows indicate the peaks discussed in the text.

the gated spectrum will still contain decays to the ground state of the  $^{17}\text{F}$ , but the decays to the excited state will be strongly enhanced. The largest relative enhancements are found for the small  $E^* \sim 4.1$  MeV peak, just above the  $p + ^{17}\text{F}$  threshold of 3.923 MeV, and for the background on either side of the wide  $E^* \sim 6.3$ -MeV peak, with the enhancement of the high-energy side being largest. Therefore, these regions appear to be dominated by decay to the first excited state. The origin of the background around the 6.3 MeV peak is not clear; we do not expect very wide excited states in this region and so it must be produced from some other background process.

As the ground and first excited states of  $^{17}\text{F}$  are expected to have little neutron strength in the  $sd$  shell, then spectroscopic factors for the proton decay of the  $^{18}\text{Ne}$  states formed by neutron capture to this shell should be very small and hence lead to narrow intrinsic widths. The only exception would be for  $J^\pi = 0^+$  states formed by filling the neutron hole in  $^{17}\text{Ne}$  where larger  $p + ^{17}\text{F}$  spectroscopic factors are possible. However the only observed  $J^\pi = 0^+$  state was close to the  $p + ^{17}\text{F}$  threshold and the barrier penetration factor should also give this state a narrow width. Shell-model calculations suggest the widths should be at most a few keV. In comparison our simulated dispersion associated with the experimental resolution has a FWHM of  $\sim 200$  keV. Thus in fitting the measured excitation-energy spectrum, we can ignore the contribution from the intrinsic widths and use these simulations to give the experimental line shapes.

The fit to the excitation-energy spectrum displayed in Fig. 12 was made using these line shapes and including two peaks for each level, one for decay to the ground state (solid lines) and a second peak, located 495 keV lower in mean energy, for a decay branch to the first excited state

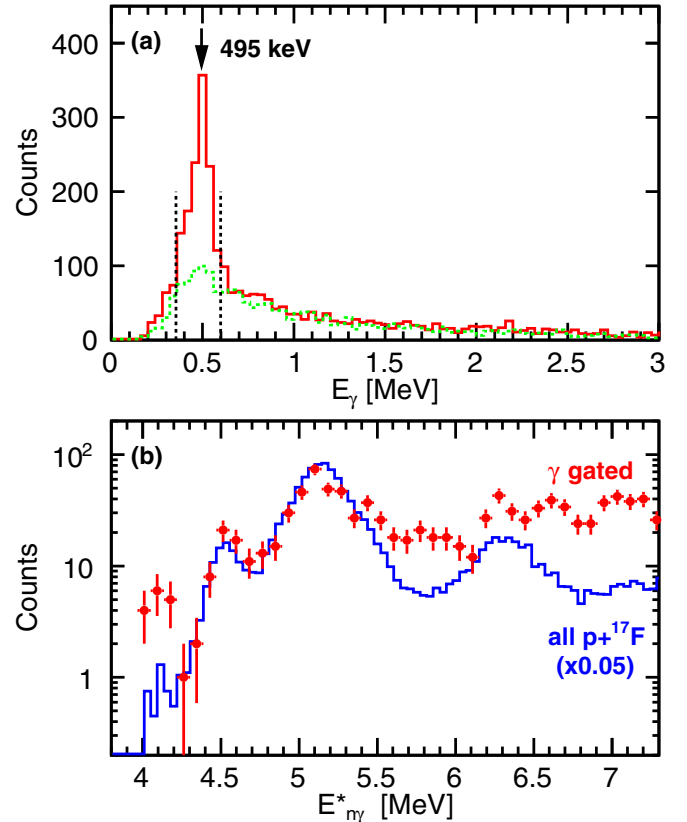


FIG. 13. (a) Spectrum of Doppler-corrected  $\gamma$  rays measured with CAESAR (with add-back contributions from neighboring detectors) in coincidence with the detected  $p + ^{17}\text{F}$  pairs showing the peak at 495 keV associated with the decay of the first excited state of  $^{17}\text{F}$ . The lower histogram shows an estimate of the background contribution, while the dashed lines indicate the outer limits of our  $\gamma$ -ray gate around the 495-keV peak. (b) The data points show the  $\gamma$ -ray-gated spectrum of  $E_{\gamma}^*$  for detected  $p + ^{17}\text{F} + \gamma$  events which is compared to the histogram for all detected  $p + ^{17}\text{F}$  pairs. Both spectra were obtained with  $|\cos(\theta)| < 0.7$ .

(dashed curves). Peaks for these latter decays are not resolved in most cases, but we can extract maximum yields for these decays consistent with data. The results we obtain are probably an overestimation of these excited-state branches as other sources of background are present. In addition, there is overlap of some of these unresolved peaks and thus in the fits we consider the contributions from only one of these at a time in obtaining these limiting values. The energy, cross section, and limiting branching ratio obtained from these fits are listed in Table IV.

To help interpret the results we have performed shell-model calculations in the  $sp\text{sd}pf$  space with the WBP interaction [36] using the code OXBASH [37]. Branching ratios were calculated from the shell-model spectroscopic factors using single-particle reduced decay widths calculated with a Coulomb plus a Wood-Saxon nuclear potential of radius parameter  $r_0 = 1.25$  fm and diffuseness 0.65 fm with its depth adjusted to get the correct resonance energy.

TABLE IV. Parameters obtained from the fit to the excitation-energy spectrum of  $^{18}\text{Ne}$  in Fig. 12. The quantity  $E_{n\gamma}^*$  is the centroid of the peak in the spectrum while  $E_{\text{level}}$  is the energy of the decaying level. These energies are different when the decay is to the first excited state of  $^{17}\text{F}$ . The assigned spin parity of the level is given by  $J^\pi$ , while  $\sigma_{\text{peak}}$  is the cross section of the peak in the fit. Experimental and theoretical branching ratios for the decay to the first excited state of  $^{17}\text{F}$  are also listed.

$E_{n\gamma}$ (MeV)	$E_{\text{level}}$ (MeV)	$J^\pi$	$\sigma_{\text{peak}}$ ( $\mu\text{b}$ )	$\Gamma_{J^\pi=1/2^+}^*/\Gamma_{\text{tot}}$ expt.	$\Gamma_{J^\pi=1/2^+}^*/\Gamma_{\text{tot}}$ theory
4.099(12)	4.594(12)	$0_3^+$	11(3)	$>0.16^{\text{b}}$	0.036
4.514(4)	4.514(4)	$1_1^-$	133(8)	$<0.125^{\text{b}}$	$1.32 \times 10^{-6}$
5.135(2)	5.135(1)	$3_1^-$	1206(20)	$<0.009^{\text{b}}$	$3.6 \times 10^{-4}$
5.457(8)	5.457(8)	$2_1^-$	186(13)	$<0.19^{\text{b}}$	0.0022
6.150 <sup>a</sup>	6.150 <sup>a</sup>	$1_2^-$	$<54^{\text{b}}$	$0.65^{\text{c}}$	
$\sim 6.3$	$\sim 6.3$	$(2_2^-, 3_2^-)$	354(17)	$<0.12^{\text{b}}$	

<sup>a</sup>Fixed to value from [18].

<sup>b</sup> $2\sigma$  limit.

<sup>c</sup>Fixed to value from [35].

#### A. 4.099-MeV peak

The lowest-energy peak observed in Fig. 12 is about 200 keV above the 3.923-MeV threshold for the  $p + ^{19}\text{F}$  decay channel. From Fig. 13, we argued that this peak is associated with decay to the first excited state of  $^{17}\text{F}$  rather than the ground state like the other observed peaks. Given that the decay energy to the ground state is much larger ( $\sim 700$  keV above threshold) one might expect its smaller barrier penetration factor would kill any significant decay branch to the excited state unless this state had some special structure.

Including the  $\gamma$ -ray energy (495 keV), our peak corresponds to a level at  $E^* = 4.594(12)$  MeV which is consistent with the energy of the  $J^\pi = 0_3^+$  level measured by Nero *et al.* (see Sec. VIB). The structure of the lowest three  $0^+$  states in  $^{18}\text{Ne}$  can be gauged from studies of their analogs in  $^{18}\text{O}$ . Fortune and Hadley argue that these states have proton  $(1s_{1/2})^2$  and  $(0d_{5/2})^2$  components as well as a collective  $4p-2h$  contribution [38]. They also indicate that the wave function for the third of these states is dominated by the  $(1s_{1/2})^2$  contribution which will give a large spectroscopic factor for the  $p + ^{17}\text{F}_{J^\pi=1/2^+}^*$  decay channel. Of course the  $(0d_{5/2})^2$  component will be associated with decay to the  $J^\pi = 5/2^+$  ground state of  $^{17}\text{F}$ . In addition to the larger spectroscopic factor for decay to the excited state, this mode will be further enhanced by a smaller centrifugal barrier;  $\ell = 0$  compared to  $\ell = 2$  for ground-state decay. Both of these two properties conspire to counter the effect of the small decay energy and give a significant branch to the excited state. However we expect that decay to the ground state is also significant. Yield from such a branch would produce an enhancement to the high-energy tail of the 4.514-MeV peak (Sec. VIB). With the maximum amount of this contribution allowed in our fit, we conclude that the minimum branching ratio to the first excited state is 16% at the  $2\sigma$  level.

Our shell-model predictions give a value of 3.6% for this branching ratio using the level energy 4.950(8) MeV listed

in [18]. The calculated branching ratio is quite sensitive to this energy, with its value increasing to 7.6% if the energy is increased by twice its statistical uncertainty. However it is still smaller than the experimental lower limit of 16% suggesting that the relative contribution of  $(1s_{1/2})^2$  to  $(0d_{5/2})^2$  of 5.5 is underestimated in these shell-model calculations. In the work of Fortune and Hadley, the strengths of the different configurations in the  $0^+$  wave functions were constrained using experimental data giving a  $(1s_{1/2})^2$  to  $(0d_{5/2})^2$  ratio of 14.4 for this state. This is a factor of 2.6 larger than our shell-model calculations and allows for consistency with our experimental limit.

The shell model predicts a large spectroscopic factor of  $C^2S(p_{1/2}) = 0.66$  for neutron capture to the  $p_{1/2}$  level. However the larger momentum mismatch for  $p$ -wave capture should suppress the yield of this case relative to those for  $d$ -wave capture. We measured a cross section of  $13(3) \mu\text{b}$  for the proton decay branch to the first excited state of  $^{17}\text{F}$ . However, based on the minimum limit for this branching ratio in Table IV, the total cross section for this state must be less than  $81 \mu\text{b}$ . This is more than a factor of 15 smaller than the yield for the 5.135-MeV,  $J^\pi = 3_1^-$  state (Sec. VIC) which has a predicted spectroscopic factor of similar magnitude, but is associated with  $d$ -wave capture. This result is thus consistent with a large suppression due to the momentum mismatch.

#### B. 4.514-MeV peak

Nero *et al.* [39] reported a doublet at  $E^* \sim 4.5$  MeV. In the  $^{16}\text{O}(^3\text{He}, n)^{18}\text{Ne}$  reaction, the level energies were determined as 4.513(13) and 4.587(13) MeV while in the  $^{20}\text{Ne}(p, t)^{18}\text{Ne}$  reaction they are 4.522(10) and 4.592(10) MeV, respectively. Nero *et al.* concluded that the lower-energy member is  $J^\pi = 1_1^-$  while the higher-energy member is  $J^\pi = 0_3^+$ . Our peak at  $E^* = 4.514(4)$  MeV is thus consistent with the  $J^\pi = 1_1^-$  level.

Although we list a limit of 12.5% for the excited-state branching ratio, the actual value is expected to be extremely small as decay to the excited state is only 97 keV above threshold compared to 592 keV for ground-state decay. The shell-model estimate is  $\sim 10^{-6}$ .

The  $n + ^{17}\text{Ne}$  spectroscopic factor predicted for this state is large, however the shell-model calculations suggested it should be largely due to  $s$ -wave capture [ $C^2S(d_{3/2}) = 0.015$ ,  $C^2S(s_{1/2}) = 0.365$ ] and thus should be suppressed due to the larger momentum mismatch. Either the effect of the momentum mismatch is not as large as we expect or these shell-model predictions are in error.

#### C. 5.135-MeV peak

The dominant peak in the excitation-energy spectrum of Fig. 12 occurs at 5.135(2) MeV. Nero *et al.* [39] reported on a doublet at  $E^* \sim 5.1$  MeV using data from two reactions. In the  $^{16}\text{O}(^3\text{He}, n)^{18}\text{Ne}$  reaction, the level energies were determined as 5.075(13) and 5.135(25) MeV, while in the  $^{20}\text{Ne}(p, t)^{18}\text{Ne}$  reaction they are 5.099(10) and 5.151(10) MeV. From angular distributions measured in that work and also by Falk *et al.* [40], one of these states was

determined to be a  $J^\pi = 2_3^+$  and the other a  $J^\pi = 3_1^-$ , but which one is the  $2_3^+$ , and conversely, which one is the  $3_1^-$  was unknown.

In order to reproduce the measured intrinsic widths of these states, Hahn *et al.* [9] subsequently argued that the higher-energy state is  $J^\pi = 3_1^-$ , while the lower-energy state is  $J^\pi = 2_3^+$ . This is in contrast to Wiescher *et al.* [41] and Funck *et al.* [42,43] who put these states in reverse order in their  $^{14}\text{O}(\alpha, p)^{17}\text{F}$  rate calculations for astrophysics.

If these two peaks were both present in our data, our energy resolution would not be sufficient to separate them, however given that this reaction is not expected to excite the  $J^\pi = 2^+$  level significantly, we conclude that the peak observed at  $E^* = 5.135(2)$  MeV is associated predominantly with the  $J^\pi = 3_1^-$  state. With our  $\pm 6.6$ -keV systematic uncertainty (Sec. II), its energy is consistent with only the higher-energy member of the doublet as measured by Nero *et al.* and thus with the spin order given by Hahn *et al.* In the shell-model calculations, this state has the largest spectroscopic factor for neutron capture to a  $d$  level [ $C^2S = 0.65$  ( $d_{5/2}$ )] and therefore it is not surprising that it is the strongest state populated in this reaction.

Almaraz-Calderon *et al.* observed a peak at a similar energy [ $E^* = 5.10(10)$  MeV] in the  $^{16}\text{O}(^3\text{He}, n)$  reaction but did not have enough resolution to separate the two members of the doublet if they both were present. They measured a branching ratio to the first excited state of  $^{17}\text{F}$  of 0.110 which is large compared to our upper limit of 0.009. The  $J^\pi = 2_3^+$  member would have to have a large branching ratio and contributed significantly to their observed peak to be consistent with our results. However, our shell-model calculations suggest that this  $2^+$  state has a very small branching ratio of 0.002.

#### D. 5.457-MeV peak

A state is resolved on the higher-energy side of the dominant 5.135-MeV peak in Fig. 12 at 5.457(8) MeV. This energy is consistent with a level at 5.453(10) MeV measured by Nero *et al.* in the  $^{20}\text{Ne}(p, t)$  reaction [39]. However, no other information on this level was determined due to its low population in that work. Hahn *et al.* list a level at 5.454 MeV as  $J^\pi = 2_1^-$  based on Coulomb-energy shifts and angular distributions in two transfer reactions, but mostly the fact that the analogs of all other  $^{18}\text{O}$  excited states in this energy region have all been identified except for this  $J^\pi = 2_1^-$  state. The observation of a 5.457(8)-MeV state in the present work confirms this assignment. The shell-model calculations also suggest that this state has a strong  $n + ^{17}\text{Ne}$  spectroscopic factor with  $C^2S(d_{5/2}) = 0.23$  and  $C^2S(d_{3/2}) = 0.12$ .

#### E. 6.3-MeV peak

The second-most intense peak seen in Fig. 12 occurs at approximately 6.3 MeV with a width that is larger than the predicted experimental resolution for this energy. Assuming that the intrinsic widths of all states in this region are very small, then this peak must be a multiplet. Hahn *et al.* list three negative-parity levels in this energy region that could be excited in our reaction [9]; a  $J^\pi = 3^-, 2^-$  doublet at

$E^* = 6.286$  and  $6.345$  MeV, and in addition the  $J^\pi = 1^-$  level at  $E^* = 6.15$  MeV that can contribute to the low-energy tail. For this latter state, He *et al.* determined that the excited-state and ground-state decay branches are approximately equal [44], while Blackmon *et al.* measured  $\Gamma_{J=1/2^+}^*/\Gamma_{\text{tot}} = 0.73$  [35]. In addition our shell-model calculations also give a large branching ratio,  $\Gamma_{J=1/2^+}^*/\Gamma_{\text{tot}} = 0.65$ . With such values, any ground-state-decay yield that makes a significant contribution to the low-energy side of the 6.3-MeV peak will produce too much yield in the  $E^*$  region associated with excited-state decay. Thus we conclude that this level does not contribute significantly to the observed peak.

The fit shown in Fig. 12 was obtained as the sum of two peaks of similar intensities with energies of 6.279(36) and 6.369(36) MeV which are consistent with the energies of the aforementioned doublet listed by Hahn *et al.* The spin order of this doublet is not well determined, but the preference of Hahn *et al.* is the opposite order to that for the analog states in  $^{18}\text{O}$  (see Fig. 11). In Table IV we list only the total cross section and the average branching ratio for these two states.

#### F. Branching ratios

The extracted limits to the branching ratios to the first excited state of  $^{17}\text{F}$  are listed in Table IV and compared to values from our shell-model calculations. Some of these cases have already been discussed in the previous sections. Apart from the 4.594-MeV  $J^\pi = 0_3^+$  state, our maximum limits are all much larger than, and thus consistent with, the theoretical values. The only other negative-parity state which is expected to have a significant branching ratio, the 6.150-MeV  $J^\pi = 1_2^-$  level [35,44], was not resolved in this work but may contribute to the enhanced yield of the  $\gamma$ -ray gated yield in Fig. 13(b) between the 5.349- and 6.3-MeV peaks.

#### G. Other exit channels

Apart from the  $p + ^{17}\text{F}$  exit channel, we have also observed three peaks in the  $\alpha + ^{14}\text{O}$  and  $2p + \alpha + ^{12}\text{C}$  invariant-mass distributions which correspond to higher-lying excited states. The extracted level information is listed in Table V and the decay of the states are illustrated in the level diagram in Fig. 14. No evidence of these levels has been observed in other decay channels, though the  $p + ^{17}\text{F}$  decay channel in particular will have low efficiency and poor resolution so our sensitivity is significantly reduced.

TABLE V. Mean excitation energies  $E^*$ , intrinsic widths  $\Gamma$ , and cross sections of states obtained from fitting the  $^{18}\text{Ne} \rightarrow \alpha + ^{14}\text{O}$  decay spectrum in Fig. 15 and the  $^{18}\text{Ne} \rightarrow 2p + \alpha + ^{12}\text{C}$  decay spectrum in Fig. 16(a).

$E^*$ (MeV)	Channel	$\Gamma$ (keV)	$\sigma_{\text{peak}}$ ( $\mu\text{b}$ )
9.111(25)	$\alpha + ^{14}\text{O}$	$<60^a$	52(5)
11.584(64)	$\alpha + ^{14}\text{O}$	$<650^a$	$\sim 18$
16.794(29)	$2p + \alpha + ^{12}\text{C}$	328(68)	182(11)

<sup>a</sup> $1\sigma$  limit.

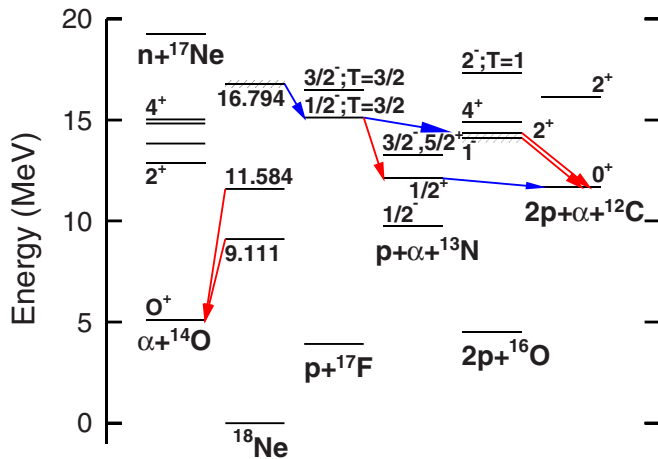


FIG. 14. Level diagram for  $^{18}\text{Ne}$  and the neighboring nuclei showing the decay of the three new states associated with the  $\alpha + ^{14}\text{O}$  and  $2p + \alpha + ^{12}\text{C}$  channels.

The excitation-energy distribution from the  $\alpha + ^{14}\text{O}$  channel is shown in Fig. 15. A rather narrow level ( $\Gamma < 60$  keV) is observed at 9.111(25) MeV and a higher-energy peak is also present at 11.58(64) MeV. The lower-energy peak was not observed in an  $\alpha + ^{14}\text{O}$  elastic scattering experiment, where an  $E^* = 9.2$ -MeV level was found, but its width is much larger ( $\Gamma = 300$  keV) [45]. The presence of the wider peak at almost the same energy may have reduced their sensitivity to the level we observed, but on the other hand, with its small decay width, it may not have a strong  $\alpha$ -cluster structure and thus was not strongly excited in the  $\alpha$ -scattering experiment.

For highly fragmented decay channels, it can be difficult to determine the decay path as there are many possible intermediate states and it becomes especially difficult if there are multiple decay paths as is the case for the peak in the  $2p + \alpha + ^{12}\text{C}$  channel. The invariant-mass spectrum for this channel, shown as the black circular data points in Fig. 16(a), contains a peak at 16.794(20) MeV. Due to the low statistics, no transverse gate has been applied. After selecting events

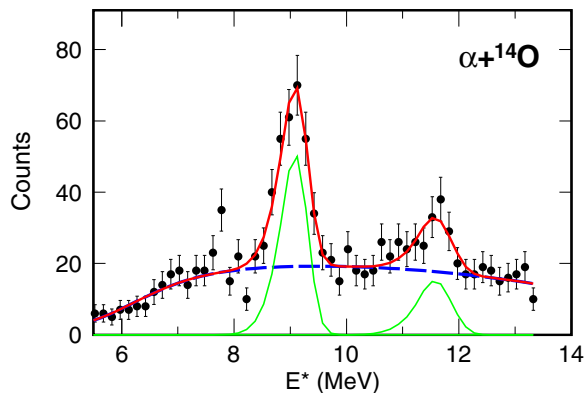


FIG. 15. Experimental  $^{18}\text{Ne}$  excitation-energy distribution for transverse  $\alpha + ^{14}\text{O}$  decays. The solid red curve shows a fit to this data with the smooth fitted background (dashed-blue curve) and the individual peaks are indicated by the solid green curves.

in this peak [gate G18 in Fig. 16(a)], the excitation-energy spectra of the various possible intermediate states are plotted in Figs. 16(b)–16(e) as the magenta triangular data points. As there are two possible protons to construct the potential  $^{17}\text{F} \rightarrow p + \alpha + ^{12}\text{C}$  and  $^{13}\text{N} \rightarrow p + ^{12}\text{C}$  intermediate states, we have determined the excitation energy using each of these protons in turn, i.e., these spectra were incremented twice for each event. For comparison, the arrows show the locations of the energy levels listed in the ENSDF database [18]. Of the possible intermediate states, one stands out very clearly: the  $1/2_1^+$ , first excited state of  $^{13}\text{N}$  at  $E^* = 2.365$  in Fig. 16(e). To confirm this state is associated with the peak and not the  $\sim 30\%$  background under the peak, we have gated on the  $^{13}\text{N}$  peak [gate G13 in Fig. 16(e)] and the corresponding  $^{18}\text{Ne}$  spectrum is shown as the red-square data points in Fig. 16(a). The fitted yield in this new gated  $^{18}\text{Ne}$  spectrum is about half of the ungated version if smooth backgrounds (dashed curves) are assumed in fits. Thus we conclude that the  $^{18}\text{Ne}$  level has at least two decay pathways, one of which decays in a manner that produces the  $1/2_1^+$   $^{13}\text{N}$  intermediate state and one that does not.

Let us concentrate on the decay pathway through the  $J^\pi = 1/2_1^+$   $^{13}\text{N}$  state first. If the  $^{18}\text{Ne}$  state decays via a series of sequential decay steps, then in order to pass through this  $^{13}\text{N}$  intermediate state, it must first decay to a  $^{17}\text{F}$  or  $^{14}\text{O}$  intermediate state. See the level schemes of these and other nuclei of interest in Fig. 14. To search for such states, we have further applied the G13 gate on the  $^{17}\text{F}$  and  $^{14}\text{O}$  excitation-energy spectra in Figs. 16(b) and 16(d) (red-square data points). For the  $^{17}\text{F}$  case, this gated yield is peaked around the energy of the known isobaric analog state (IAS) ( $T = 3/2$ ,  $J^\pi = 1/2^-$ ,  $\Gamma = 0.18$  keV) at  $E^* = 11.192$  MeV. The solid curve through these data points is a simulation of the detector response of this narrow state which reproduces its shape very well. Thus we conclude that this decay pathway is described by an initial proton decay to the  $^{17}\text{F}_{\text{IAS}}$  which subsequently  $\alpha$  decays to the  $^{13}\text{N}$  state, which then proton decays to the ground state of  $^{12}\text{C}$ .

Given that this new  $^{18}\text{Ne}$  state has a strong proton-decay branch to a high- $T$  state in  $^{17}\text{F}$ , it is quite probable that this new  $^{18}\text{Ne}$  state is itself high  $T$ , i.e.,  $T = 2$  in this case. Its excitation energy is appropriate for it to be an analog of a low-lying state in  $^{18}\text{Na}$  (see later). If the second decay pathway involves a second decay branch of  $^{18}\text{Ne}$ , then to conserve isospin and energy, it should be a proton decay to the next analog state in  $^{17}\text{F}$  at  $E^* = 12.550$  MeV ( $J^\pi = 3/2^-$ ). However, the latter decay is only  $\sim 300$  keV above threshold and will be suppressed by the small Coulomb penetration factor. In addition we do not see any indication of significant yield for this intermediate state in Fig. 16(b). Thus it is more likely that the second decay pathway involves a second decay branch of  $^{17}\text{F}_{\text{IAS}}$ . Note that  $^{17}\text{F}_{\text{IAS}}$  itself has no isospin-allowed particle decay modes which are above threshold, so we expect all of its decay branches to violate isospin symmetry.

We have dismissed the possibility that this second decay branch of  $^{17}\text{F}_{\text{IAS}}$  is an  $\alpha$  decay to higher-lying states of  $^{13}\text{N}$  as there is no indication of any significant yield for such states in Fig. 16(e). Thus we restrict ourselves to a proton decay branch to either the  $1_2^-$ ,  $2_2^+$ , or  $4_1^+$  excited state in  $^{16}\text{O}$ . As such, we have simulated the decay of the  $^{18}\text{Ne}$  state as

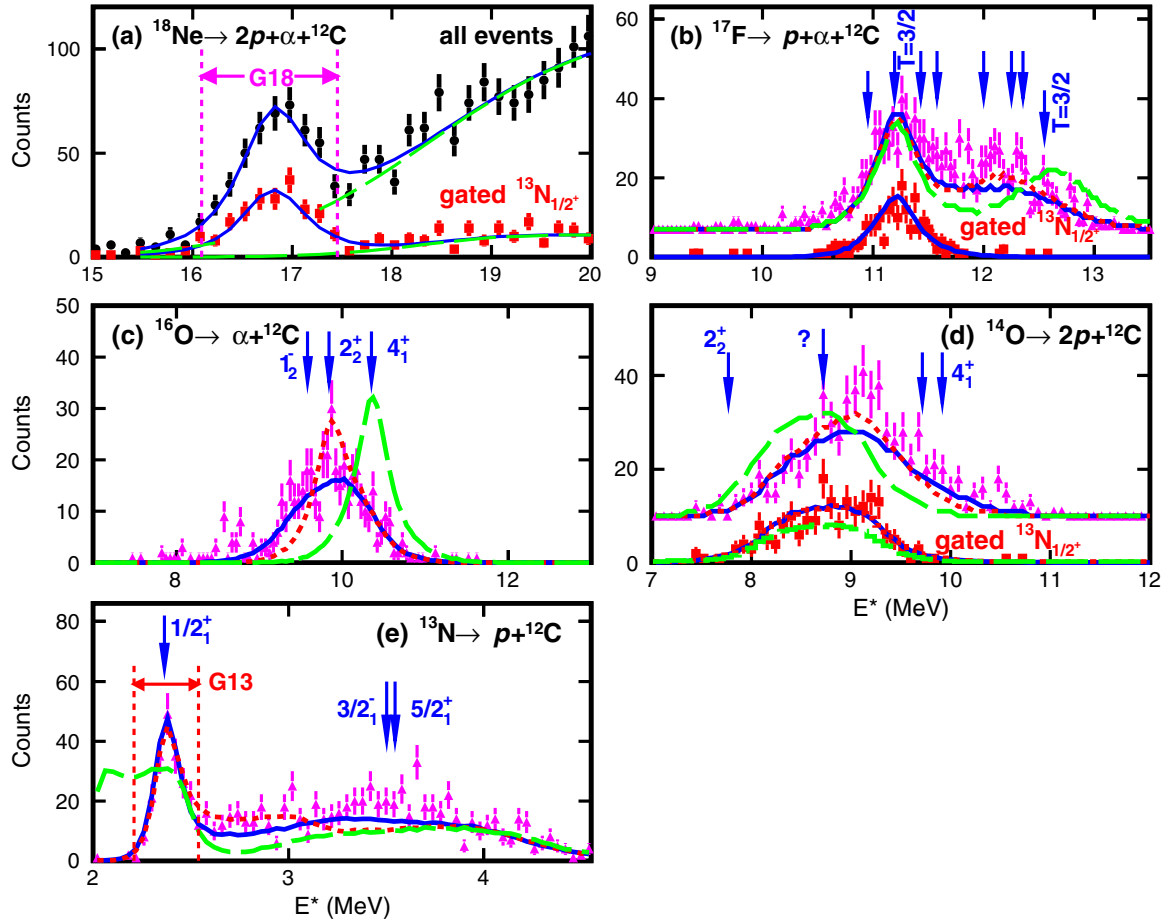


FIG. 16. Experimental invariant-mass spectra obtained from  $2p + \alpha + {}^{12}\text{C}$  events. (a) The black-circular data points show the  ${}^{18}\text{Ne}$  excitation-energy distribution for all events (no transverse gate) while the red-square data have a gate requiring an  ${}^{13}\text{N}_{1/2^+}$  intermediate state was present. The solid-blue curves are fits to the data where the fitted smooth backgrounds are shown by the dashed-green curves. (b)–(e), The magenta triangular data are invariant-mass distributions of possible intermediate states gated on the observed  ${}^{18}\text{Ne}$  peak [gate G18 in (a)]. Arrows mark the location of states listed in the ENSDF database [18]. The data in (b) and (d) have been shifted along the y axis for clarity. The red-square data in these two panels have an extra gate [gate G13 in (e)] applied. The solid-blue, red-dotted, and green-dashed curves are predictions from a simulation where the IAS in  ${}^{17}\text{F}$  has a second decay branch to either the  $J^\pi = 1/2^-, 2/2^-,$  or  $4/1^+$  excited state in  ${}^{16}\text{O}$ .

an initial proton decay to  ${}^{17}\text{F}_{\text{IAS}}$ , followed by either another proton decay to one of these three  ${}^{16}\text{O}$  intermediate states or alternatively an  $\alpha$  decay to the  $J^\pi = 1/2_1^+$   ${}^{13}\text{N}$  intermediate state, with these latter intermediate states subsequently decaying to give the  $2p + \alpha + {}^{12}\text{C}$  exit channel. For each possible  ${}^{16}\text{O}$  intermediate, the  $p/\alpha$  branching ratio of  ${}^{17}\text{F}_{\text{IAS}}$  was adjusted to best fit both the gated and ungated  ${}^{18}\text{Ne}$  excitation-energy spectra in Fig. 16(a). The simulated  ${}^{17}\text{F}$ ,  ${}^{16}\text{O}$ ,  ${}^{14}\text{O}$ , and  ${}^{13}\text{N}$  invariant-mass spectra are then compared to the experimental data in Figs. 16(b)–16(e) as the solid, dotted, and dashed curves respectively. As there is roughly a 30% background under the ungated  ${}^{18}\text{Ne}$  peak in Fig. 16(a), the predicted distributions should not account for the total experimental yield in these panels. Thus consistency with the experiment data occurs if these simulated distributions do not pass above the data points. In this regard, the decay through the  $4_1^+$   ${}^{16}\text{O}$  intermediate state (green-dashed curves) can be discarded. The simulation for the  $1_2^-$  state (solid-blue curves) is consistent with all distributions, while for the  $2_2^+$  state

(magenta-dotted curve), the curve in Fig. 16(c) overshoots the experiments distribution by roughly 30–50% at its peak. Thus the second decay branch of  ${}^{17}\text{F}_{\text{IAS}}$  involves proton decay to the  $1_2^-$   ${}^{16}\text{O}$  state, but we cannot rule out an additional smaller branch to the  $2_2^+$  state and smaller yields for other decay paths. The fitted branching ratio of  ${}^{17}\text{F}_{\text{IAS}}$  is  $\Gamma_\alpha/\Gamma_p = 0.65(9)$ .

For an isospin multiplet, the mass excesses are expected to be well described by the isospin multiplet mass equation (IMME) [46],

$$M(T, T_Z) = a + bT_Z + cT_Z^2, \quad (3)$$

where  $a$ ,  $b$ , and  $c$  are constants. Except for a few cases, deviations from the quadratic  $T_Z$  dependence are quite small. For the  $A = 18$ ,  $T = 2$  multiplets, only a few cases have at least three members known to constrain the three constants. In Fig. 17 we show quadratic IMME fits to the  $J^\pi = 2_1^-$  and  $3_1^-$  members using mass excesses determined for  ${}^{18}\text{Na}$  from [47]. For the  ${}^{18}\text{O}$ , and  ${}^{18}\text{N}$  members, we have used ground-state

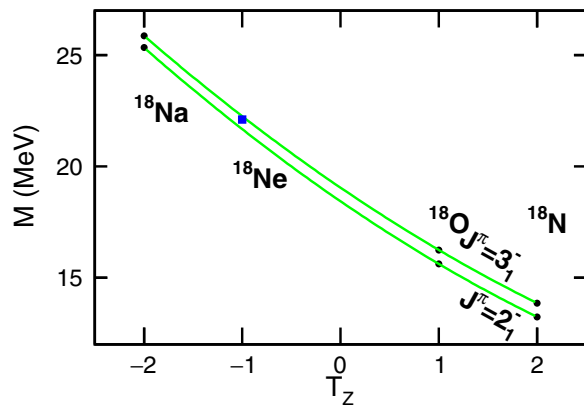


FIG. 17. Known mass excesses of the  $J^\pi = 2^-$  and  $3^-$ ,  $A = 8$ ,  $T = 2$  multiplets are plotted as the circular data points. The curves are fits with the IMME [Eq. (3)]. The location of the  $^{18}\text{Ne} \rightarrow 2p + \alpha + ^{12}\text{C}$  state is shown by the blue square.

masses from the AME2016 tabulation [48] and excitation energies from [18,49]. For comparison, the location of the new  $^{18}\text{Ne}$  peak is shown as the blue square data point. It is closer to the fitted curve for  $J^\pi = 3^-$  levels, but 140(34) keV below. Generally we expect deviation from the IMME to be much smaller than this, so probably the observed peak is not purely from this level in  $^{18}\text{Ne}$ . Indeed the fitted intrinsic width of this state is relatively large,  $\Gamma = 328(68)$  keV, significantly larger than that of the  $3^-$  state in  $^{18}\text{Na}$  [ $\Gamma = 42(10)$  keV [47]]. In  $^{18}\text{Na}$ , a very wide state [ $\Gamma = 900(100)$  keV] was observed  $\sim 50$  keV below this  $3^-$  state while a very narrow state ( $\Gamma < 1$  keV) was observed  $\sim 100$  keV below. It is possible that the observed peak is a multiplet with contributions from a number of  $^{18}\text{Ne}$  levels in this energy region.

### VII. $^{10}\text{C}$ EXCITED STATES

The ground state of  $^{9}\text{C}$  is  $J^\pi = 3/2^-$ . This is mostly a  $p$ -shell nucleus and the transfer of another neutron into the  $p$  shell will populate  $J^\pi = 0^+, 1^+, 2^+$ , and  $3^+$  states in  $^{10}\text{C}$ . At higher excitation energies, negative-parity levels can be populated by adding the extra neutron to the  $sd$  shell.

The ground and first excited states of  $^{10}\text{C}$  are particle bound and at  $E^* = 3.73$  MeV, the  $2p + 2\alpha$  decay channel opens up. This is the only available final exit channel for particle decay until  $E^* = 15.0$  MeV when the  $^3\text{He} + ^7\text{Be}$  channel is available. A number of invariant-mass studies have investigated  $2p + 2\alpha$  exit channels produced in the inelastic excitation of a  $^{10}\text{C}$  beam [50–53]. Numerous states were observed whose decay is initiated by either by  $p$ ,  $\alpha$ , or direct two-proton emission. In all the cases, the remnant nucleus undergoes further particle emission producing the observed exit channel. Many of the states are expected to have large  $\alpha$ -particle cluster structure like that of the ground-state configuration.

The  $2p + 2\alpha$  and  $^3\text{He} + ^7\text{Be}$  excitation-energy spectra obtained in the neutron pick reactions of this work are displayed in Fig. 18. The results for the  $2p + 2\alpha$  channel in Fig. 18(a) are consistent with that obtained at the same bombarding energy and target in Ref. [3] and is dominated by a state at  $E^* = 9.69$  MeV. This previous work also identified smaller

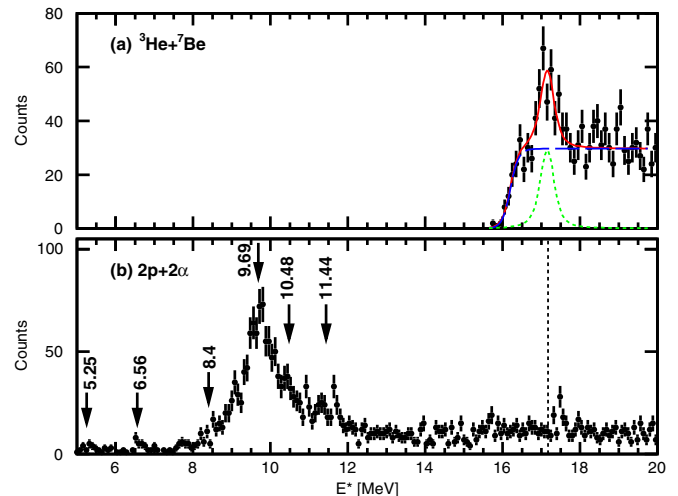


FIG. 18. Excitation-energy spectra obtained for (a) the  $2p + 2\alpha$  and (b) the  $^3\text{He} + ^7\text{Be}$  exit channels of  $^{10}\text{C}$ . For the four-body exit channel in (a), all detected  $2p + 2\alpha$  events are included, while in (b), only the transverse decays ( $|\cos\theta| < 0.2$ ) are used in constructing the spectrum. A fit to the  $^3\text{He} + ^7\text{Be}$  data is shown as the solid-red line in (b), where the individual Breit-Wigner peaks (modified by the detector resolution) are indicated by the dotted-green curve. The dashed-blue curve is an estimate of the background. The arrows in (a) show the location of peaks identified in Refs. [3,53].

peaks at  $E^* = 10.48(20)$  and  $11.44(20)$  MeV as indicated by the arrows in Fig. 18(a). These secondary peaks are not so obvious in the present data, but our statistics are lower making them more difficult to discern if present. In addition the location of the  $2p + 2\alpha$  peaks observed in the  $^{10}\text{C}$  inelastic excitation studies are also indicated by the arrows in Fig. 18(a); a doublet at  $E^* \sim 5.25$  MeV, a triplet  $E^* \sim 6.56$  MeV, and a broader peak at  $E^* = 8.4(1)$  MeV. Such peaks are either significantly suppressed or not observed in this work, consistent with their presumed strong cluster structure. The stronger yield of the 9.69-MeV state indicates it has a more shell-model-like structure.

In Ref. [3], the 9.69-MeV state was shown to have  $\alpha + ^6\text{Be}_{\text{g.s.}}$  and  $p + ^9\text{B}_{2.34\text{ MeV}}$  decay branches in addition to a more unusual branch where the  $\alpha$ - $\alpha$  relative energy is consistent with the  $J^\pi = 2^+$   $^8\text{Be}$  resonance, all the  $p$ - $\alpha$  relative energies are consistent with  $^5\text{Li}_{\text{g.s.}}$  resonances, and the  $p$ - $p$  relative energy is small reminiscent of a diproton final-state interaction. We presume this state is produced from neutron transfer to the  $p$  shell and is thus either  $J = 0^+, 1^+, 2^+$ , or  $3^+$ . Indeed the emission of a  $p$ -shell proton should leave the system in a negative-parity state consistent with the significant proton decay branch (17%) to the  $J^\pi = 5/2^-$ ,  $E^* = 2.34$  MeV state of  $^9\text{B}$  [3].

Based on the known levels in the mirror nucleus  $^{10}\text{Be}$ , the most likely analog is the 9.64-MeV,  $J^\pi = 2^+$  state. Note that we are using the excitation energy from Refs. [53–55] rather than the compiled value of  $E^* = 9.560$  MeV [18]. The width of our  $^{10}\text{C}$  peak ( $\Gamma = 490$  keV [3]) is of similar magnitude but larger than the value of  $\Gamma = 141$  keV [18] for the  $J = 2^+$  level in the mirror system which is not unreasonable as the

TABLE VI. Mean excitation energies  $E^*$ , intrinsic widths  $\Gamma$ , and cross sections obtained for the  $^{10}\text{C}$  levels observed in Fig. 18.

$E^*$ (MeV)	Channel	$\Gamma$ (keV)	$\sigma_{\text{peak}}$ ( $\mu\text{b}$ )
9.69 <sup>a</sup>	$2p + 2\alpha$	490 <sup>a</sup>	369(73)
17.17(4)	$^3\text{He} + ^7\text{Be}$	221(117)	6.9(13)

<sup>a</sup>From Ref. [3].

proton-rich member of a mirror pair of levels in the continuum generally has a larger width.

The  $^3\text{He} + ^7\text{Be}$  excitation energy-energy spectrum for transverse decay, shown in Fig. 18(b), is dominated by a single peak at  $E^* \sim 17$  MeV. This peak is associated with decay to the ground state of  $^7\text{Be}$  as no enhancement of the 429-keV  $\gamma$  rays associated with the first excited state of  $^7\text{Be}$  was observed in CAESAR. The solid-red curve shows a fit to the experimental data with a Breit-Wigner-shaped peak (modified by the detector resolution) and the blue-dashed curve is the fitted background contribution. Fitted parameters are listed in Table VI. The fitted peak energy is  $E^* = 17.17(4)$  MeV with an intrinsic width consistent with zero [ $\Gamma = 57(256)$  keV]. There are no known states in the mirror system  $^{10}\text{Be}$  close to this energy so no assignment to analog states can be made at present.

In Fig. 18(a) there is no indication of any decay branch of this state to the  $2p + 2\alpha$  channel (see dotted line for the energies of the fitted level). However at such large decay energies, the detection efficiency of the  $2p + 2\alpha$  channel is very small as many of the decay fragments are emitted outside the angular acceptance of the HiRA. The simulated efficiency of detecting all four particles is a factor of 6 smaller than the  $^3\text{He} + ^7\text{Be}$  result with the transverse decay cut ( $|\cos\theta| < 0.2$ ). Combined with a larger simulated experimental resolution (FWHM 700 keV), it is possible that this peak contributes to the observed mostly flat background at large energies in Fig. 18(a) and thus we cannot rule out that this state also has a non-negligible branching ratio to the  $2p + 2\alpha$  channel.

### VIII. CONCLUSION

We have used invariant-mass spectroscopy with the HiRA and CAESAR arrays to study excited states in the continuum produced in neutron-transfer reactions to fast secondary beams of  $^9\text{C}$ ,  $^{15}\text{O}$ , and  $^{17}\text{Ne}$ . With the thick  $^9\text{Be}$  target, which was selected to produce adequate yields with the low beam rates, the experimental resolution was found to be very sensitive to the orientation of the decay axis of these states. For two-body decays in particular, the best resolution was found for events where the decay axis is perpendicular to the beam direction. Here the uncertainty associated with energy losses of the decay products in leaving the target material are minimized. These transfer reactions were found to leave the remnant target nucleons with large excitation energies. Further studies are needed to understand this, but at present this excludes the extraction of spectroscopic factors from comparisons with DWBA calculations.

With the  $^{17}\text{Ne}$  beam, we have confirmed the spin assignments made by Hahn *et al.* [9] for a number of  $^{18}\text{Ne}$  excited states. In addition we have found new excited states in  $^{16}\text{O}$  and  $^{18}\text{Ne}$  at high excitation energies. Some of these decays are highly fragmented with up to four particles in the continuum. This includes an exotic fission mechanism for  $^{16}\text{O}$  states resulting in two  $^8\text{Be}_{g.s.}$  fragments. A newly found high- $T$  state in  $^{18}\text{Ne}$  was observed to decay to the isobaric analog state in  $^{17}\text{F}$ . The latter was also found to have isospin nonconserving  $\alpha$  and proton decay branches. Finally a new excited state in the  $^{10}\text{C}$  was also found.

This work demonstrates the usefulness of invariant-mass spectroscopy in transfer reaction with fast fragmentation beams. Unfortunately, cross sections are typically much smaller than other simple reaction mechanisms such as knock-out or inelastic excitation. However, as in the present work, transfer data can be obtained in concert with data from other reactions.

### ACKNOWLEDGMENTS

We thank Prof. Alex Brown for lessons on using the OXBASH code. This material is based upon work supported by the U.S. Department of Energy, Office of Science, Office of Nuclear Physics under Awards No. DE-FG02-87ER-40316, No. DE-FG02-04ER-41320, and No. DE-SC0014552 and the NSF under Grant No. PHY-156556. K.W.B. was supported by a National Science Foundation Graduate Fellowship under Grant No. DGE-1143954 and J.M. was supported by a Department of Energy National Nuclear Security Administration Steward Science Graduate Fellowship under cooperative Agreement No. DE-NA0002135.

### APPENDIX: MONTE CARLO SIMULATIONS

The experimental resolution and detection efficiency were determined from Monte Carlo simulations of the reactions which incorporated the following effects.

- (1) The energy loss of the beam particle and decay fragments in the target material were taken from Ref. [16]. The reaction is assumed to occur randomly in depth within the limits of the physical target.
- (2) Small-angle scattering of the beam particle and decay fragments in the target material following Ref. [56].
- (3) The effect of a realistic beam spot size ( $\sim 1$  cm diameter) and the known momentum acceptance of the secondary beam are included.
- (4) The angle resolution associated with the pixel size of the Si strip  $\Delta E$  detectors is included.
- (5) The energy resolution of the CsI(Tl) detectors is estimated based on our calibration beams.
- (6) The detection efficiency includes the loss due to nuclear reactions of the incident particles with the Cs and I nuclei in the  $E$  detector [57,58].
- (7) The intrinsic line shapes of resonances were taken to have a Breit-Wigner form with the centroid and width adjusted in the fits unless otherwise specified.

The Monte Carlo events produced by the simulation are analyzed in the same manner as the experimental data. The ingredients in the simulations were fine tuned by fitting known narrow resonances. For example, the  $p + ^{17}\text{F}$  resolution was fine tuned by fitting the  $2p + ^{15}\text{O}$  resonance peak associated with the decay of the second excited state of  $^{17}\text{Ne}$  as discussed in the [4,6]. Both transverse and longitudinal decays are considered as these have sensitivities to different ingredients. For the fission of  $^{16}\text{O}$  states into two  $^8\text{Be}_{\text{g.s.}}$  fragments producing a final exit channel of four  $\alpha$  particles, three resonances were used for fine tuning. These are the  $^8\text{Be}_{\text{g.s.}} \rightarrow 2\alpha$  resonance plus the  $3\alpha$  resonances associated with the  $^{12}\text{C}$  second (Hoyle state) and third ( $J^\pi = 3^-$ ) excited states.

Input primary angular and velocity distributions of the parent fragments formed in the transfer reactions were adjusted so that reconstructed secondary distributions (obtained from the decay fragments after the effects of the detector acceptance and resolution are incorporated) match their experimental counterparts. For asymmetric exit channels like  $p + ^{17}\text{F}$ , there is an uncertainty in extrapolating to zero degrees as the detection efficiency vanishes here and this adds uncertainty to our final cross sections. However, as the  $d\sigma/d\theta$  must vanish as one approaches zero degrees, this uncertainty is not large. We estimate this uncertainty is less than 15%. For the  $^{16}\text{O}$  fission channels, this zero degree region is sampled by the experimental events so a similar problem does not exist.

- [1] M. S. Wallace, M. A. Famiano, M.-J. van Goethem, A. M. Rogers, W. G. Lynch, J. Clifford, F. Delaunay, J. Lee, S. Labostov, M. Mocko, L. Morris, A. Moroni, B. E. Nett, D. J. Oostdyk, R. Krishnasamy, M. B. Tsang, R. T. de Souza, S. Hudan, L. G. Sobotka, R. J. Charity *et al.*, The high resolution array (HiRA) for rare isotope experiments, *Nucl. Instrum. Methods Phys. Res. A* **583**, 302 (2007).
- [2] R. J. Charity, J. M. Elson, J. Manfredi, R. Shane, L. G. Sobotka, Z. Chajecski, D. Coupland, H. Iwasaki, M. Kilburn, J. Lee, W. G. Lynch, A. Sanetullaev, M. B. Tsang, J. Winkelbauer, M. Youngs, S. T. Marley, D. V. Shetty, A. H. Wuosmaa, T. K. Ghosh, and M. E. Howard,  $2p$ - $2p$  decay of  $^8\text{C}$  and isospin-allowed  $2p$  decay of the isobaric analog state in  $^8\text{B}$ , *Phys. Rev. C* **82**, 041304(R) (2010).
- [3] R. J. Charity, J. M. Elson, J. Manfredi, R. Shane, L. G. Sobotka, B. A. Brown, Z. Chajecski, D. Coupland, H. Iwasaki, M. Kilburn, J. Lee, W. G. Lynch, A. Sanetullaev, M. B. Tsang, J. Winkelbauer, M. Youngs, S. T. Marley, D. V. Shetty, A. H. Wuosmaa, T. K. Ghosh, and M. E. Howard, Investigations of three-, four-, and five-particle decay channels of levels in light nuclei created using a  $^9\text{C}$  beam, *Phys. Rev. C* **84**, 014320 (2011).
- [4] K. W. Brown, R. J. Charity, L. G. Sobotka, Z. Chajecski, L. V. Grigorenko, I. A. Egorova, Yu. L. Parfenova, M. V. Zhukov, S. Bedoor, W. W. Buhro, J. M. Elson, W. G. Lynch, J. Manfredi, D. G. McNeel, W. Reviol, R. Shane, R. H. Showalter, M. B. Tsang, J. R. Winkelbauer, and A. H. Wuosmaa, Observation of Long-Range Three-Body Coulomb Effects in the Decay of  $^{16}\text{Ne}$ , *Phys. Rev. Lett.* **113**, 232501 (2014).
- [5] K. W. Brown, W. W. Buhro, R. J. Charity, J. M. Elson, W. Reviol, L. G. Sobotka, Z. Chajecski, W. G. Lynch, J. Manfredi, R. Shane, R. H. Showalter, M. B. Tsang, D. Weisshaar, J. R. Winkelbauer, S. Bedoor, and A. H. Wuosmaa, Two-proton decay from the isobaric analog state in  $^8\text{B}$ , *Phys. Rev. C* **90**, 027304 (2014).
- [6] K. W. Brown, R. J. Charity, L. G. Sobotka, L. V. Grigorenko, T. A. Golubkova, S. Bedoor, W. W. Buhro, Z. Chajecski, J. M. Elson, W. G. Lynch, J. Manfredi, D. G. McNeel, W. Reviol, R. Shane, R. H. Showalter, M. B. Tsang, J. R. Winkelbauer, and A. H. Wuosmaa, Interplay between sequential and prompt two-proton decay from the first excited state of  $^{16}\text{Ne}$ , *Phys. Rev. C* **92**, 034329 (2015).
- [7] K. W. Brown, R. J. Charity, J. M. Elson, W. Reviol, L. G. Sobotka, W. W. Buhro, Z. Chajecski, W. G. Lynch, J. Manfredi, R. Shane, R. H. Showalter, M. B. Tsang, D. Weisshaar, J. R. Winkelbauer, S. Bedoor, and A. H. Wuosmaa, Proton-decaying states in light nuclei and the first observation of  $^{17}\text{Na}$ , *Phys. Rev. C* **95**, 044326 (2017).
- [8] R. A. Leavitt, H. C. Evans, G. T. Ewan, H.-B. Mak, R. E. Azuma, C. Rolfs, and K. P. Jackson, Isospin mixing in  $2^-$  levels in  $^{16}\text{O}$ , *Nucl. Phys. A* **410**, 93 (1983).
- [9] K. I. Hahn, A. García, E. G. Adelberger, P. V. Magnus, A. D. Bacher, N. Bateman, G. P. A. Berg, J. C. Blackmon, A. E. Champagne, B. Davis, A. J. Howard, J. Liu, B. Lund, Z. Q. Mao, D. M. Markoff, P. D. Parker, M. S. Smith, E. J. Stephenson, K. B. Swartz, S. Utku, R. B. Vogelaar, and K. Yildiz, Structure of  $^{18}\text{Ne}$  and the breakout from the hot CNO cycle, *Phys. Rev. C* **54**, 1999 (1996).
- [10] K. A. Chippis, D. W. Bardayan, C. D. Nesaraja, M. S. Smith, J. C. Blackmon, K. Y. Chae, B. H. Moazen, S. T. Pittman, U. Greife, R. Hatarik, W. A. Peters, R. L. Kozub, J. F. Shriner, C. Matei, and S. D. Pain, The  $^{17}\text{F}(p, \gamma)^{18}\text{Ne}$  resonant cross section, *Phys. Rev. C* **80**, 065810 (2009).
- [11] J. Hu, J. J. He, A. Parikh, S. W. Xu, H. Yamaguchi, D. Kahl, P. Ma, J. Su, H. W. Wang, T. Nakao, Y. Wakabayashi, T. Teranishi, K. I. Hahn, J. Y. Moon, H. S. Jung, T. Hashimoto, A. A. Chen, D. Irvine, C. S. Lee, and S. Kubono, Examination of the role of the  $^{14}\text{O}(\alpha, p)^{17}\text{F}$  reaction rate in type-I x-ray bursts, *Phys. Rev. C* **90**, 025803 (2014).
- [12] D. M. Brink, Kinematical effects in heavy-ion reactions, *Phys. Lett. B* **40**, 37 (1972).
- [13] A. Gade, P. Adrich, D. Bazin, M. D. Bowen, B. A. Brown, C. M. Campbell, J. M. Cook, T. Glasmacher, K. Hosier, S. McDaniel, D. McGlinchery, A. Obertelli, L. A. Riley, K. Siwek, J. A. Tostevin, and D. Weisshaar, Inverse-kinematics one-proton pickup with intermediate-energy beams: The  $^9\text{Be}(^{20}\text{Ne}, ^{21}\text{Na} + \gamma)X$  reaction, *Phys. Rev. C* **76**, 061302(R) (2007).
- [14] A. Gade, J. A. Tostevin, T. Baugher, D. Bazin, B. A. Brown, C. M. Campbell, T. Glasmacher, G. F. Grinyer, S. McDaniel, K. Meierbachtol, A. Ratkiewicz, S. R. Stroberg, K. A. Walsh, D. Weisshaar, and R. Winkler, Inverse-kinematics one-neutron pickup with fast rare-isotope beams, *Phys. Rev. C* **83**, 054324 (2011).
- [15] A. Gade, J. A. Tostevin, V. Bader, T. Baugher, D. Bazin, J. S. Berryman, B. A. Brown, D. J. Hartley, E. Lunderberg, F. Recchia, S. R. Stroberg, Y. Utsuno, D. Weisshaar, and K. Wimmer, One-neutron pickup into  $^{49}\text{Ca}$ : Bound neutron  $g_{9/2}$  spectroscopic strength at  $N = 29$ , *Phys. Rev. C* **93**, 031601(R) (2016).

- [16] J. F. Ziegler, J. P. Biersack, and U. Littmark, *The Stopping and Range of Ions in Solids* (Pergamon, New York, 1985); the code SRIM can be found at [www.srim.org](http://www.srim.org).
- [17] D. Weisshaar, A. Gade, T. Glasmacher, G. F. Grinyer, D. Bazin, P. Adrich, T. Baugher, J. M. Cook, C. Aa. Diget, S. McDaniel, A. Ratkiewicz, K. P. Siwek, and K. A. Walsh, CAESAR high-efficiency CsI(Na) scintillator array for in-beam spectroscopy with fast rare-isotope beams, *Nucl. Instrum. Methods Phys. Res. A* **624**, 615 (2010).
- [18] Evaluated Nuclear Structure Data File (ENSDF), <http://www.nndc.bnl.gov/ensdf/>.
- [19] W. Bohne, H. Homeyer, H. Lettau, H. Morgenstern, J. Scheer, and F. Sichelschmidt, Study of states in  $^{16}\text{O}$  by the reactions  $^{17}\text{O}(t, \alpha)^{16}\text{O}$  and  $^{15}\text{N}(t, d)^{16}\text{O}$ , *Nucl. Phys. A* **160**, 257 (1971).
- [20] W. Bohne, J. Bommer, H. Fuchs, K. Grabisch, H. Kluge, and G. Röscher, Study of the  $(d, n)$  and  $(d, p)$  reactions on  $^{15}\text{N}$ , *Nucl. Phys. A* **196**, 41 (1972).
- [21] F. Ajzenberg-Selove, Energy levels of light nuclei  $A = 16$ -17, *Nucl. Phys. A* **281**, 1 (1977).
- [22] C. Rolfs and W. S. Rodney, Proton capture by  $^{15}\text{N}$  at stellar energies, *Nucl. Phys. A* **235**, 450 (1974).
- [23] F. Zijderhand and C. van der Leun, Strong M2 transitions, *Nucl. Phys. A* **460**, 181 (1986).
- [24] A. A. Kraus, A. P. French, W. A. Fowler, and C. C. Lauritsen, Angular distribution of gamma-rays and short-range alpha-particles from  $\text{N}^{15}(p, \alpha\gamma)\text{C}^{12}$ , *Phys. Rev.* **89**, 299 (1953).
- [25] K. H. Bray, A. D. Frawley, T. R. Ophel, and F. C. Barker, Levels of  $^{16}\text{O}$  near 13 MeV excitation from  $^{15}\text{N} + p$  reactions, *Nucl. Phys. A* **288**, 334 (1977).
- [26] D. F. Hebbard, Proton capture by  $\text{N}^{15}$ , *Nucl. Phys.* **15**, 289 (1960).
- [27] P. Chevallier, F. Scheibling, G. Goldring, I. Plessner, and M. W. Sachs, Breakup of  $\text{O}^{16}$  into  $\text{Be}^8 + \text{Be}^8$ , *Phys. Rev.* **160**, 827 (1967).
- [28] F. Brochard, P. Chevallier, D. Disdier, V. Rauch, G. Rudolf, and F. Scheibling,  $^{12}\text{C}(\alpha, ^8\text{Be})^8\text{Be}$  reaction in the energy range  $E_\alpha = 17$ -33 MeV, *Phys. Rev. C* **13**, 967 (1976).
- [29] A. H. Wuosmaa, Many-particle decays of a  $\alpha$ -chain structures in  $^{24}\text{Mg}$ , *Z. Phys. A* **349**, 249 (1994).
- [30] M. Freer, N. M. Clarke, N. Curtis, B. R. Fulton, S. J. Hall, M. J. Leddy, J. S. Pople, G. Tungate, R. P. Ward, P. M. Simmons, W. D. M. Rae, S. P. G. Chappell, S. P. Fox, C. D. Jones, D. L. Watson, G. J. Gyapong, S. M. Singer, W. N. Catford, and P. H. Regan,  $^8\text{Be}$  and  $\alpha$  decay of  $^{16}\text{O}$ , *Phys. Rev. C* **51**, 1682 (1995).
- [31] M. Freer, M. P. Nicoli, S. M. Singer, C. A. Bremner, S. P. G. Chappell, W. D. M. Rae, I. Boztosun, B. R. Fulton, D. L. Watson, B. J. Greenhalgh, G. K. Dillon, R. L. Cowin, and D. C. Weissner,  $^8\text{Be} + ^8\text{Be}$  decay of excited states in  $^{16}\text{O}$ , *Phys. Rev. C* **70**, 064311 (2004).
- [32] A. Soylu, M. Freer, N. I. Ashwood, N. Curtis, T. Munoz-Britton, S. Spencer, C. Wheldon, V. Ziman, S. Brown, J. S. Thomas, G. Wilson, and G. Goldring, Excitation function measurements of  $^{12}\text{C}(^4\text{He}, ^8\text{Be})^8\text{Be}$ ,  $^{12}\text{C}(^4\text{He}, ^{12}\text{C}[7.65, 0^+])^4\text{He}$ , and  $^{12}\text{C}(^4\text{He}, ^{12}\text{C}[9.64, 3^-])^4\text{He}$  reactions, *Phys. Rev. C* **86**, 057601 (2012).
- [33] N. Curtis, S. Almaraz-Calderon, A. Aprahamian, N. I. Ashwood, M. Barr, B. Bucher, P. Copp, M. Couder, X. Fang, M. Freer, G. Goldring, F. Jung, S. R. Leshner, W. Lu, J. D. Malcolm, A. Roberts, W. P. Tan, C. Wheldon, and V. A. Ziman, Investigation of the  $4\text{-}\alpha$  linear chain state in  $^{16}\text{O}$ , *Phys. Rev. C* **88**, 064309 (2013).
- [34] H. T. Fortune, R. Sherr, and B. A. Brown, Coulomb energies in  $^{17}\text{Ne}$  and the ground state mass of  $^{18}\text{Na}$ , *Phys. Rev. C* **73**, 064310 (2006).
- [35] J. C. Blackmon, D. W. Bardayan, W. Bradfield-Smith, R. Brummitt, A. E. Champagne, A. A. Chen, T. Davinson, L. Dessieux, M. W. Guidry, K. I. Hahn, G. M. Hale, W. R. Hix, R. L. Kozub, Z. Ma, P. D. Parker, G. Rajbaidya, R. C. Runkle, C. M. Rowland, A. C. Shotter, M. S. Smith, L. A. Van Wormer, D. W. Visser, and P. J. Woods, The  $^{14}\text{O}(\alpha, p)^{17}\text{F}$  reaction rate, *Nucl. Phys. A* **718**, 127 (2003).
- [36] B. A. Brown, The nuclear shell model towards the drip lines, *Prog. Part. Nucl. Phys.* **47**, 517 (2001).
- [37] B. A. Brown, A. Etchegoyen, N. S. Godwin, W. D. M. Rae, W. A. Richter, W. E. Ormand, E. K. Warburton, J. S. Winfield, L. Zhao, and C. H. Zimmerman, Technical Report MSU-NSCL-1289 (National Superconducting Cyclotron Laboratory, Michigan State University, East Lansing, MI, 2004).
- [38] H. T. Fortune and S. C. Headley, Structure of  $0^+$  states in  $^{18}\text{O}$ , *Phys. Lett. B* **51**, 136 (1974).
- [39] A. V. Nero, E. G. Adelberger, and F. S. Dietrich, Structure of  $^{18}\text{Ne}$ , *Phys. Rev. C* **24**, 1864 (1981).
- [40] W. R. Falk, R. J. Kidney, P. Kulisic, and G. K. Tandon, Energy levels of  $^{18}\text{Ne}$  from the  $^{20}\text{Ne}(p, t)^{18}\text{Ne}$  reaction, *Nucl. Phys. A* **157**, 241 (1970).
- [41] M. Wiescher, V. Harms, J. Görres, F.-K. Thielemann, and L. J. Rybarczyk, Alpha-burning of  $^{14}\text{O}$ , *Astrophys. J.* **316**, 162 (1987).
- [42] C. Funck and K. Langanke, Microscopic study of the  $^{14}\text{O}(\alpha, p)^{17}\text{F}$  reaction at stellar energies, *Nucl. Phys. A* **480**, 188 (1988).
- [43] C. Funck, B. Grund, and K. Langanke, Improved study of the  $^{14}\text{O}(\alpha, p)^{17}\text{F}$  reaction at stellar energies, *Z. Phys. A* **332**, 109 (1989).
- [44] J. J. He, P. J. Woods, T. Davinson, M. Aliotta, J. Büscher, E. Clement, P. Delahaye, M. Hass, D. G. Jenkins, V. Kumar, A. St. J. Murphy, P. Neyskens, R. Raabe, A. P. Robinson, D. Voulot, J. van der Walle, N. Warr, and F. Wenander, Measurement of the inelastic branch of the  $^{14}\text{O}(\alpha, p)^{17}\text{F}$  reaction: Implications for explosive burning in novae and x-ray bursters, *Phys. Rev. C* **80**, 042801(R) (2009).
- [45] C. Fu, V. Z. Goldberg, G. V. Rogachev, G. Tabacaru, G. G. Chubarian, B. Skorodumov, M. McCleskey, Y. Zhai, T. Al-Abdullah, L. Trache, and R. E. Tribble, First observation of  $\alpha$ -cluster states in the  $^{14}\text{O} + ^4\text{He}$  interaction, *Phys. Rev. C* **77**, 064314 (2008).
- [46] M. MacCormick and G. Audi, Evaluated experimental isobaric analog states from  $T = 1/2$  to  $T = 3$  and associated IMME coefficients, *Nucl. Phys. A* **925**, 61 (2014).
- [47] M. Assié, F. de Oliveira Santos, T. Davinson, F. de Grancey, L. Achouri, J. Alcántara-Núñez, T. Al Kalanee, J.-C. Angélique, C. Borcea, R. Borcea, L. Caceres, I. Celikovic, V. Chudoba, D. Y. Pang, C. Ducoin, M. Fallot, O. Kamalou, J. Kiener, Y. Lam, A. Lefebvre-Schuhl *et al.*, Spectroscopy of  $^{18}\text{Na}$ : Bridging the two-proton radioactivity of  $^{19}\text{Mg}$ , *Phys. Lett. B* **712**, 198 (2012).
- [48] M. Wang, G. Audi, F. G. Kondev, W. J. Huang, S. Naimi, and X. Xu, The AME2016 atomic mass evaluation (II). Table, graphs and references, *Chin. Phys. C* **41**, 030003 (2017).
- [49] C. R. Hoffman, M. Albers, M. Alcorta, S. Almaraz-Calderon, B. B. Back, S. I. Baker, S. Bedoor, P. F. Bertone, B. P. Kay, J. C. Lighthall, T. Palchan, R. C. Pardo, G. Perdikakis,

- K. E. Rehm, A. M. Rogers, D. Santiago-Gonzalez, Cenxi Yuan, and J. P. Schiffer, Single-neutron excitations in  $^{18}\text{N}$ , *Phys. Rev. C* **88**, 044317 (2013).
- [50] R. J. Charity, K. Mercurio, L. G. Sobotka, J. M. Elson, M. Famiano, A. Banu, C. Fu, L. Trache, and R. E. Tribble, Decay of  $^{10}\text{C}$  excited states above the  $2p + 2\alpha$  threshold and the contribution from “democratic” two-proton emission, *Phys. Rev. C* **75**, 051304(R) (2007).
- [51] K. Mercurio, R. J. Charity, R. Shane, L. G. Sobotka, J. M. Elson, M. Famiano, A. H. Wuosmaa, A. Banu, C. Fu, L. Trache, R. E. Tribble, and A. M. Mukhamedzhanov, Correlated two-proton decay from  $^{10}\text{C}$ , *Phys. Rev. C* **78**, 031602(R) (2008).
- [52] N. Curtis, N. L. Achouri, N. I. Ashwood, H. G. Bohlen, W. N. Catford, N. M. Clarke, M. Freer, P. J. Haigh, B. Laurent, N. A. Orr, N. P. Patterson, N. Soić, J. S. Thomas, and V. Ziman, Breakup reaction study of the Brunnian nucleus  $^{10}\text{C}$ , *Phys. Rev. C* **77**, 021301(R) (2008).
- [53] R. J. Charity, S. A. Komarov, L. G. Sobotka, J. Clifford, D. Bazin, A. Gade, J. Lee, S. M. Lukyanov, W. G. Lynch, M. Mocko, S. P. Lobastov, A. M. Rogers, A. Sanetullaev, M. B. Tsang, M. S. Wallace, R. G. T. Zegers, S. Hudan, C. Metelko, M. A. Famiano, A. H. Wuosmaa, and M. J. van Goethem, Investigation of particle-unbound excited states in light nuclei with resonance-decay spectroscopy using a  $^{12}\text{Be}$  beam, *Phys. Rev. C* **78**, 054307 (2008).
- [54] S. Hamada, M. Yasue, S. Kubono, M. H. Tanaka, and R. J. Peterson, Cluster structures in  $^{10}\text{Be}$  from the  $^7\text{Li}(\alpha, p)^{10}\text{Be}$  reaction, *Phys. Rev. C* **49**, 3192 (1994).
- [55] N. Soić, S. Blagus, M. Bogovac, S. Fazinić, M. Lattuada, M. Milin, D. Miljanić, D. Rendić, C. Spitaleri, T. Tadić, and M. Zadro,  $^6\text{He} + \alpha$  clustering in  $^{10}\text{Be}$ , *Europhys. Lett.* **34**, 7 (1996).
- [56] R. Anne, J. Herault, R. Bimbot, H. Gauvin, C. Bastin, and F. Hubert, Multiple angular scattering of heavy ions ( $^{16,17}\text{O}$ ,  $^{40}\text{Ar}$ ,  $^{86}\text{Kr}$ ,  $^{100}\text{Mo}$ ) at intermediate energies (20-90 MeV/u), *Nucl. Instrum. Methods Phys. Res. B* **34**, 295 (1988).
- [57] R. J. Charity, L. G. Sobotka, N. J. Robertson, D. G. Sarantites, J. Dinius, C. K. Gelbke, T. Glasmacher, D. O. Handzy, W. C. Hsi, M. J. Huang, W. G. Lynch, C. P. Montoya, G. F. Peaslee, C. Schwarz, and M. B. Tsang, Prompt and sequential decay processes in the fragmentation of 40 MeV/nucleon  $^{20}\text{Ne}$  projectiles, *Phys. Rev. C* **52**, 3126 (1995).
- [58] P. Morfouace, W. G. Lynch, and M. B. Tsang, Charged-particle detection efficiencies of close-packed CsI arrays, *Nucl. Instrum. Methods Phys. Res. A* **848**, 45 (2017).